Mário André Madeira de Almeida

Licenciatura em Química Aplicada – Ramo Orgânica

Photoluminescent properties of doped alkali borosilicate glasses

Dissertação para obtenção do Grau de Mestre em Química Bioorgânica

Orientador: Andreia Ruivo, Investigadora Auxiliar, Faculdade de Ciência e Tecnologia

Co-orientador: Hugo Àguas, Professor Associado, Faculdade de Ciência e Tecnologia

Júri:

Presidente: Prof. Doutora Ana Maria Ferreira da Costa Lourenço

Arguente(s): Dr. Manuel João de Moura Dias Mendes

Vogais: Dra. Andreia Filipa Cardoso Ruivo

FACULDADE DE CIÊNCIAS E TECNOLOGIA
UNIVERSIDADE NOVA DE LISBOA

Setembro, 2017

Mário André Madeira de Almeida

Licenciatura em Química Aplicada – Ramo Orgânica

Photoluminescent properties of doped alkali borosilicate glasses

Dissertação para obtenção do Grau de Mestre em Química Bioorgânica

Orientador: Andreia Ruivo, Investigadora Auxiliar, Faculdade de Ciência e Tecnologia

Co-orientador: Hugo Àguas, Professor Associado, Faculdade de Ciência e Tecnologia

Júri:

Presidente: Prof. Doutora Ana Maria Ferreira da Costa Lourenço

Arguente(s): Dr. Manuel João de Moura Dias Mendes

Vogais: Dra. Andreia Filipa Cardoso Ruivo

FACULDADE DE CIÊNCIAS E TECNOLOGIA
UNIVERSIDADE NOVA DE LISBOA

Setembro, 2017

Photoluminescent properties of doped alkali borosilicate glasses

Agradecimentos

Primeiramente agradeço aos meus orientadores de mestrado Andreia Ruivo e Professor Hugo Àguas, pela orientação dada, disponibilidade permanente e paciência para as minhas inúmeras dúvidas. Extendo estas palavras de agradecimento ao Professor César Laia, desde o primeiro dia que o seu apoio é fundamental, incansável e inspirador. Ainda, um muito obrigado ao investigador Prashant Dabas por ter sempre a sua porta aberta para tantas dúvidas que lhe coloquei.

Agradeço ainda a oportunidade de colaboração com o projecto *From inexpensive raw materials to new luminescent glass materials,* que se extende às unidades de investigação parceiras ao seu desenvolvimento, nomeadamente a unidade de investigação de vidro e cerâmica, VICARTE da Faculdade de Ciências e Tecnologia da Universidade Nova de Lisboa, onde passei muito do meu tempo neste último ano, e também à unidade de investigação CICECO do Instituto de materiais da Universidade de Aveiro. Extendo estes agradecimentos institucionais ao CENIMAT e ao Departamento de Materiais da Faculdade de Ciências e Tecnologia da Universidade Nova de Lisboa.

Agradeço ao departamento de Fotoquímica, Professor Fernando Pina, Professor Jorge Parola, Professor João Lima, e ao grupo que é extraordinário. Desde que entrei pela vossa porta que fui acolhido como se estivesse em casa. Obrigado a todos vós pela oportunidade de aprender convosco, pela vossa solidariedade, honestidade e amizade.

Agradeço aos meus pais, Manuel e Alice, por me fazerem tão livre quanto um dia sonhei ser, à minha irmã Marta por tanto me dar, ainda que sem o saber, à minha família que está sempre presente e aos meus amigos que me cobram por saudades que eu também sinto deles.

À Mariana, pelos seus sorrisos infinitos.

Esta tese de mestrado teve o apoio financeiro providenciado pelo projecto *From inexpensive raw materials to new luminescent glass materials,* PTDC/QEQ-QIN/3007/2014.

Abstract

This project was developed with the purpose to achieve innovative solutions of UV light down conversion. Such was accomplished through the synthesis of photoluminescent glasses doped with tin oxide and copper oxide, also preliminary studies on the development of photoluminescent thin films based on the same elements was approached. Photoluminescent quantum yields and Stokes shift were taken as guidelines to evaluate the photoluminescent behaviour of the produced samples.

The synthetic strategy applied for photoluminescent glass samples was systematic, it consisted on the insertion of a variable doping amount of each element over an alumina-borosilicate glass matrix which were prepared at high temperatures of 1400 ºC and 1550 ºC. Structural features were evaluated through SSNMR for ^{29}Si, ^{11}B, ^{23}Na, and Raman spectroscopy, which showed that doping does not affect the network structural matrix. Dilatometry measurements were performed showing a negligible variation of the thermomechanical properties of the samples.

Doping concentrations have revealed to be a key factor for the achievement of high quantum performances, where we have observed triplet state light emission derived from three emissive species. Its origin resides in Sn^{2+}, Sn^{2+} aggregates and Cu^{+} species in the glass matrix. Tin oxide doped samples shown quantum efficiencies of 50% and 1.7 eV Stokes shift for 1.4% molar tin oxide concentration, while copper oxide doped samples present 58% quantum efficiency and large 3 eV Stokes shift for 0.14% molar concentration.

Thin film deposition strategy was based on the identification of optimal conditions for the formation of copper and tin oxide crystalline phases. Results were evaluated through X-ray diffraction and Raman spectroscopy showing the formation of both crystalline phases over variable oxygen flow. A multi-layer thin film deposition was performed and diffusion was attempted through thermal treatment. Results indicate the formation of a protective SnO_2 layer over the formation of Cu_2O phase, increasing its thermal stability to 400 ºC.

Keywords: Tin Oxide, Copper Oxide, UV-Downconversion, Luminescent solar concentrators, Alumina-borosilicate glass matrix, Thin-Films.

Resumo

A investigação realizada teve como objectivo o desenvolvimento de soluções inovadoras conversão de luz UV em luz visível. O trabalho foi realizado através da síntese de vidros fotoluminescentes dopados com óxido de estanho e óxido de cobre, além de estudos preliminares de desenvolvimento de filmes finos fotoluminescentes baseados nos mesmos elementos. Eficiências quanticas de luminescencia e desvios de Stokes foram avaliados de modo a caracterizar o comportamento fotoquímico das amostras produzidas.

A estratégia de síntese aplicada no desenvolvimento dos vidros fotoluminescentes foi sistemática, consistiu na variação de concentração de dopagem de cada elemento sobre uma matriz vitrea de aluminoborosilicato preparada a altas temperaturas, 1400 ºC e 1550 ºC. A avaliação estrutural foi realizada através de ressonancia magnética nuclear dos isótopos ^{29}Si, ^{11}B, ^{23}Na, e através de espectroscopia de Raman. Os resultados indicam que o processo de dopagem não influencia a matriz estrutural do vidro. As propriedades termo-mecânicas dos vidros foram avaliadas através da técnica de dilatometria, corroborando a observação estrutural.

As concentrações de dopagem revelaram-se um fator determinante para alcançar altas eficiências quânticas para a dopagem mista, onde foi possível observar uma natureza de emissão de luz proveniente do estado tripleto de três estruturas emissivas. A sua origem provém de Sn^{2+}, agregados de Sn^{2+} e de Cu^{+} presentes na matriz vítrea. As amostras dopadas com óxido de estanho apresentam uma eficiência quântica de 50% com um desvio de Stokes de 1.7eV para concentrações de 1.4% mol de óxido de estanho. As amostras dopadas com oxide de cobre apresentam uma eficiência quântica de 58% e um desvio de Stokes de 3 eV para a concentração de 0.14% mol de cobre.

A estratégia de deposição de filmes finos baseou-se na identificação de condições optimizadas para a formação de fases cristalinas de óxido de cobre e óxido de estanho. Os resultados foram avaliados através de técnicas de difracção de raios-x e espectroscopia de Raman que demonstraram a formação de ambas as fases cristalinas através da variação de fluxo de oxigénio. Realizou-se uma deposição mista sobre a qual foi aplicado tratamento térmico com o intuito de difundir os elementos sobre o substrato. Os resultados indicam a formação de uma camada protetora de óxido de estanho sobre óxido de cobre que permitem aumentar a sua estabilidade térmica até aos 400 ºC.

Palavras-chave: Óxido de estanho, Óxido de cobre, Conversão de Luz UV em visível, Concentradores de luz solar, Matrizes vítreas de alumina-borosilicato, Filmes finos.

Index

Figure Index

Table Index

1. State of the Art

Luminescent materials have been used in a broad range of technological appliances such as fluorescent tubes of coloured televisions, x-ray photography or lasers. Historically, these technologies are commonly based on the characteristic sharp emission and very high quantum efficiencies of lanthanide ions[1]. Technological development based on rare earths has to a large extent placed society on a dependent position regarding its availability. Such represents a major concern since scarceness and availability are drastically interfering with its market value. Countermeasures have been placed in form of incentives given to provide alternative solutions, by, among others, the European Commission which has expressed a strong recommendation on the development and technological optimization of non-toxic raw materials whose supply is not at risk[2].

The interest in UV to visible light down conversion from raw materials has pulled greater attention from the scientific community ever since the development of nanocrystalline structures[3][4], quantum dots[5] and perovskites [6] which show a sharp emissive profile. The great challenge is in fact the usage of elements whose structural optimization process trigger high quantum performances[1].

Tin and copper have appeared as a suitable candidates for efficient photonic conversion in solar cells as luminescent solar concentrators (LSC)[7], solid state lighting applications (LED)[8-10] and lasers[11]. Stability of tin or copper doping of multicomponent glasses has been verified in distinct glass matrixes[12-15], where the use of multicomponent base glass, *i.e.* which include more than one network former (such as Si or B) and intermediate role elements (as Al), have shown to allow segregation and consequentially allow crystallite formation[16]. The interest of these materials in photovoltaic technology is allied to the optimization use of the light spectrum, energy harvesting in photovoltaic cells is more effective if absorbed closer to the band gap of the cells[18]. Moreover, alumina-borosilicate glasses present high chemical durability and are extremely resistant to thermal shock[17], making them excellent candidates to the development of LSC's.

Large area LSC's production might become extremely efficient through the sputtering deposition technique. Thin film deposition is performed over a host material that may be developed as rigid or flexible substrate, either transparent or opaque, suitable to the design and development of variable applications from which we highlight building applications or electronic integration use.

The major challenge in the field resides in the development of new materials or alloys in the form of thin films that could support these luminescent properties, Thin films of copper or tin oxide may possess semiconductor properties, which provide unique possibilities as active layers in solar cells, Cu_2O has a direct band gap of 2.1 eV while tin oxide has a wide and direct band gap of 3.6 eV, making them excellent candidates for large band energy conversion[19-20]. It is also possible that the confinement of small Cu_2O nanoparticles into SnO_2 may originate photoluminescent behaviour which can be incorporated onto its host substrate[8], making them up- or down-converters, which would improve the actual efficiency of solar cells[21].

The main purpose of this thesis resides on the development of innovative solutions regarding UV-light conversion through the usage of tin and copper oxide embedded in a glass matrix and deposited as a thin film.

2. Fundamentals

2.1. *Glass fundamentals*

Glass is an amorphous solid which completely lacks long range periodic atomic structure, and exhibits a region of glass transformation behaviour. James E. Shelby [22]

A glass matrix is created across short and intermediate-range bonding, constituted by distinct packing environments through a non-crystalline tri-dimensional network matrix. Such was demonstrated from radial distribution function analysis (figure 2.1), which describes how density varies as a function of distance. Crystals exhibit a sharp radial distribution with periodic density, gas show a linear-shape distribution and liquids or glasses distribution oscillate in the short radial region, converging towards a linear distribution shape in the long radial distance.

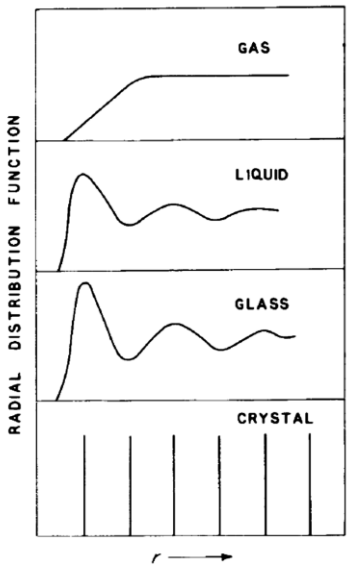

Figure 2.1 - Radial distribution function of a hypothetical material in a gas, liquid, glass, and crystalline state. *Adapted from reference (24).*

The structural formation of glass is dependent, as pointed by Turnbull[23], from the kinetics of its formation. The cooling rate required to avoid that a given volume fraction of the matrix is crystallized depends on its quenching rate. This phenomena derives from the competing driving force for crystallization (which increases with decreasing temperature), and the atomic mobility (which decreases with decreasing temperature). High temperature decreases the viscosity of the glass allowing atoms to rearrange and establish bonds to a more stable form of the matrix. As heat is taken away from the fluid, the rate of vibrational cooling is reduced and free volume is diminished. This causes a fundamental change; the fluid contracts reducing mobility (β) and increasing its density and viscosity (η) as stated by the Stokes-Einstein relation:

$$\beta = \frac{1}{6\pi\eta r} \text{ (r = atomic radius) (1)}$$

Further cooling fixes a definite structure, but in order to obtain a glass it is necessary to cool the liquid to a temperature below the limit of the crystallization (T_m). Such must be done at a rate higher than crystallization limits, otherwise we obtain crystalline phases in the glass structural matrix. The classic two variable diagram, enthalpy or volume, and temperature (Figure 2.2.) relates the cooling rate of a glass and the formation of a crystal structure.

The glass transformation range describes a metastable thermodynamic region of the material where phase transformation is reversible. This phenomena, known as hysteresis, allows the determination of the *glass transition temperature* (T_g) through the intersection of the extrapolated liquid and glass state lines. When the viscosity of a glass reaches a limit value at which it is still capable to prevent deformation derived from its own weight, it is also possible to identify the *softening temperature* (T_s)[22].

By applying heat to the material we induce variation of amplitude of the anharmonic vibration of the atomic constituents of the matrix. Its interatomic distance relation to the lattice is affected and

dependent on temperature, enabling its analysis through the determination of the coefficient of thermal expansion (CTE).[24]

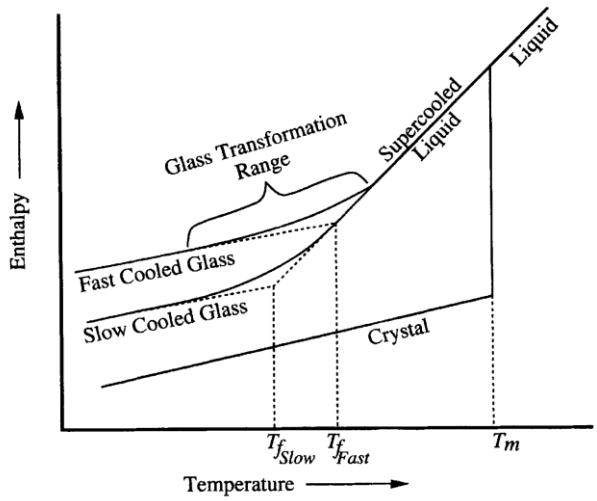

Figure 2.2 – Glass transformation range dependence on enthalpy and temperature *Adapted from reference (22)*

2.2. *Structural Role of Elements*

The choice of starting materials used to produce a specific glass is broad. Each set of elements attain specific properties as a glass with distinct mechanical, optical, or functional capabilities. Study of the individual abilities of each element is crucial for a clear assessment of the luminescent centres in the matrix and its enhancement.

The elements role in the glass matrix is dependent on atomic structure and individual glass forming abilities. A simple structural glass can be produced solely through the insertion of one primary glass former, for example silica oxide (SiO_2) or boric oxide (B_2O_3). SiO_2 assumes a predominant tetrahedric unit arrangement in a glass matrix[27], while boric oxide, B_2O_3, assumes two predominant geometries in glass, either four-coordinated tetrahedral (BO_4) or a tri-coordinated (BO_3) trigonal planar unit[28]. The energy necessary to melt a pure silica glass (~1700ºC), is however extremely high which justifies the insertion of modifiers or flux elements which reduce the glass melting temperature.

In a borosilicate glass two separate phases emerge due to the immiscibility of the boron and silica network. Network modifier elements, such as lithium (Li^+), sodium (Na^+) and potassium (K^+) act as disrupting agents whose ionic strength is sufficiently high to cleave network structural bonds (Si-O-Si or B-O-B), creating anionic non-bridging oxygen throughout the matrix (Figure 2.3). The broader effect through flux addition is the change of thermo-mechanical properties of the glass since a loosen structure has lower viscosity and glass melting range.[24]

The amount of non-bonding oxygen in the matrix can, to a certain extent, be controlled through the addition of intermediate elements. Alumina, for example, is known to add chemical and thermo-mechanical stability to a glass host[29], it will form Si-O-Al and B-O-Al bonds restoring network

connectivity and supressing phase separation[30]. Although an intermediate element is unable to form a glass by itself, it acts as a glass former when combined with other primary network formers.

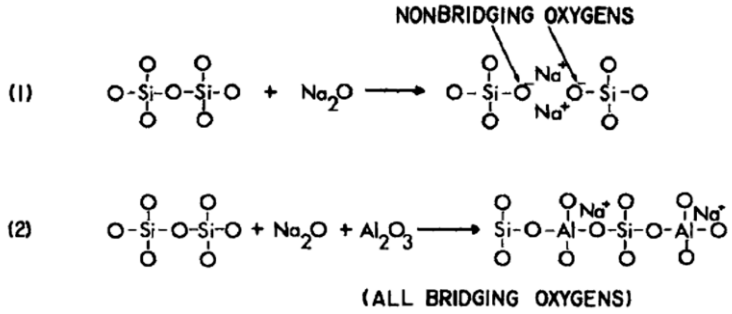

Figure 2.3 - (1) Origin of NBO ions by introducing Na_2O into the SiO_2 network (2) Alumina restores network bridging in presence of Na^+. Adapted from *reference (31)*

The concept of element role of on a glass matrix was studied by Dietzel[32], who pursuit a clear definition of the empirical role of specific elements. Based on the cation-oxygen bond energy criteria, Dietzel analysed coloumbic attractions between ionic species and correlated ionic size and polarizability in the matrix. The concept of cation field strength (F) relates the ratio between the ionic valence (Z), and the squared ionic distance for oxides ($a=r_{cation}+r_{O^{2-}}$). Further elucidation of the concept was developed by Sun[24] who analysed this classification based on atomic bond-strength.

Both approaches are intimately related, glass formers present *high* field strength (FS), and *high* single bond energy (SB), FS>1.3 and SB>80 kcal/mol. Glass modifiers show *low* field strength, F<0.4 and *low* single bond energy SB<60 kcal/mol. Intermediate values found for some elements present an *intermediate* field strength value, and *intermediate* single bond strength, 0.4<FS<1.3, SB=60-80 kcal/mol. Classification of basis set of cations that will be applied in the glass development procedure can be found on table 2.1.

Other features are attributed to elements due to their role in the glass matrix. Take the example regarding a problem associated with the most common form of insertion of a modifier element in the glass mixture:

$$Na_2CO_3 \xrightarrow{\Delta} Na_2O + CO_2 \uparrow \quad (2)$$

Usually prepared from its carbonate form, the molecule decomposes at high temperatures into sodium oxide and carbon dioxide. The gaseous rate of diffusion depends on the viscosity of the melt, physical trapping of the gas can be opposed through the residual addition of fining agents who enable viscosity reduction of the glass melt[22].

It is also of interest to refer the colorant elements, in most cases transition metals with a 3*d* electron valence shell or rare earths with a 4*f* valence shell are used, copper for example, is a well-known colorant to obtain a red ruby colour when in the oxidation state Cu^0, or green and blue colour tones when in oxidation state Cu^{2+} [23].

The oxidation state of the elements is of great importance, our interest resides in observing the luminescent properties of stannous Sn^{2+} and cuprous Cu^+ ions, for which it is of relevance to evaluate the redox ambient of the melt.

Table 2.1 - Classification of basis set of cations used in this study. Adapted from *reference (32).*

Element	Valence (Z)	Ionic Radii, Å, (CN=6) [(a)]	Coordination number (CN)	Ionic distance for oxides, Å, (a) [(b)]	Field Strength (F)	Function
Si^{4+}	4	0.4	4	1.80	1.23	Glass Formers
B^{3+}	3	0.27	3	1.67	1.07	
B^{3+}	3	0.11	4	1.50	1.31	
Al^{3+}	3	0.535	6	1.89	0.80	Intermediate
K^{+}	1	1.38	6	2.78	0.13	Glass Modifier
Na^{+}	1	1.02	6	2.42	0.17	
Li^{+}	1	0.76	6	2.16	0.21	
Sn^{2+}	2	1.18	6	2.58	0.3	Modifier
Sn^{4+}	4	0.69	6	2.09	0.9	Intermediate
Cu^{+}	1	0.77	6	2.17	0.21	Modifier
Cu^{2+}	2	0.73	6	2.13	0.44	Intermediate

[(a)] Shannon, R. D.; Acta Cryst. (1976). A32, 751.
[(b)] $r_{O^{2-}}$ = 1.4 Å when CN=6.

Electron exchange reactions between oxygen and the multivalent components of the melt are relevant for structural definition of the glass matrix. Oxygen activity is subject to thermodynamic constraints which determine its incorporation or release from the structure. Such affects the glass basicity and consequently the redox potentials. It is important to retain the idea that the inherent ability of an element to reduce a species is the overriding factor in controlling its reduction potential. Our goal is to create Cu^{+} luminescent centres which are dependent, on a great extent, of electron transfer between SnO and CuO. This reaction will take place during the melting procedure and can be described through equation 3:

$$SnO + 2CuO \rightleftharpoons SnO_2 + Cu_2O \quad (3)$$

While reduction potentials are typically determined in water at standard conditions (25°C, 1 atm), in a glass melt, subject to a distinct solvent at very high temperature values, the observation of experimental values is limited. Schreiber was able to derive from silicate glass experimental data a mathematical expression with limited maximum temperature constraints (maximum of 1150ºC) which relates the ratio of the concentrations of the element between its reduced state and oxidized state (x), the number of electrons transferred in the redox couple (n), and the imposed oxygen fugacity (fo_2) [(33)].

$$log\ x = \frac{n}{4} \times (-log\ f_{O_2}) + E. \quad (4)$$

Comparison of the standard reference values and Schreiber values, applied for the reaction $Cu^{2+} + Sn^{2+} \rightarrow Cu^{+} + Sn^{4}$ are shown in table 2.2. Nernst equation allows the calculation of the redox potential in both solvents, in water at standard conditions the reaction is spontaneous, although presenting a very low driving force: ΔG_R = -0.02 eV. The increase in spontaneity of the reaction when subject to temperature in the silica solvent is immense, with a ΔG_R = -9.4 eV. These values indicate that when in the right proportion Cu^{2+} will be fully reduced to Cu^{+} whereas the luminescent Sn^{2+} will act as a sacrificial agent whenever the redox reaction takes place.

Table 2.2 - Standard reference redox-couple potentials values in water (rt), Schreiber values for silica glass melt at 1150°C, calculated values for the for the reaction $Cu^{2+} + Sn^{2+} \rightarrow Cu^{+} + Sn^{4+}$, in water at room temperature (rt), and in silica at 1150ºC

Reaction	E^0 (V) Water, *rt*	E^0 (V) Silica, 1150ºC
$Sn^{4+} \rightarrow Sn^{2+}$	+0.14	-5.5
$Cu^{2+} \rightarrow Cu^{+}$	+0.16	-0.8
$Cu^{+} \rightarrow Cu^{0}$	+0.52	-3.3

Reaction	Calculated E^0 (V)
$Sn^{2+}+Cu^{2+} \rightarrow Sn^{4+}+Cu^{+}$	-0.02 (water, rt) -9.4 (Silica,1150 ºC)

2.3. *Photoluminescence in glass*

The study of photoluminescence describes the phenomena in which, after photon absorption, an element or molecule emits light. Photon absorption from an electron in a lower energy state, promotes it to a high energy excited state, a transition that corresponds to a change in the electronic configuration of the excited state in relation to its ground state. The excited state nature is *transient*, i.e., it loses energy after a specific amount of time. Generically speaking radiative lifetime presents two types of energy decay: (i) When the radiative decay of emission presents a short lifetime, in the order of nano-seconds, it is termed fluorescence. (ii) When the radiative decay has a long lifetime, from microseconds to seconds, it is termed phosphorescence.

Both types of energy decay derive from the Pauli principle which states that two particles must have opposite half-integer spins within the quantum system. The excited state may assume a distinct spin multiplicity in relation to its ground state. If the electronic transition presents a distinct multiplicity between ground state and excited state, it represents a forbidden transition according to the spin selection rule, and it usually exhibits a long lifetime (μs to s). When the ground state and the excited state present the same spin multiplicity, luminescence decay is allowed according to the spin selection rule, and it exhibits a short lifetime (ns).

Comparison between the electronic nature of both excited and ground state allow the evaluation of the reorganization energy, or the Stokes-shift. However, not only through light emission can the excited state relaxation proceed, its deactivation may also be accomplished through thermal energy release to the surrounding medium. This competitive mechanism of luminescence deactivation has distinct origins: (i) thermal vibrational processes, (ii) excited state redox reactions or (iii) non-radiative energy transfer[58].

If a kinetic rate constant (k) is associated with each radiative and non-radiative process, the following Jablonski diagram may be presented in order to describe the above-mentioned phenomena, figure 2.4.

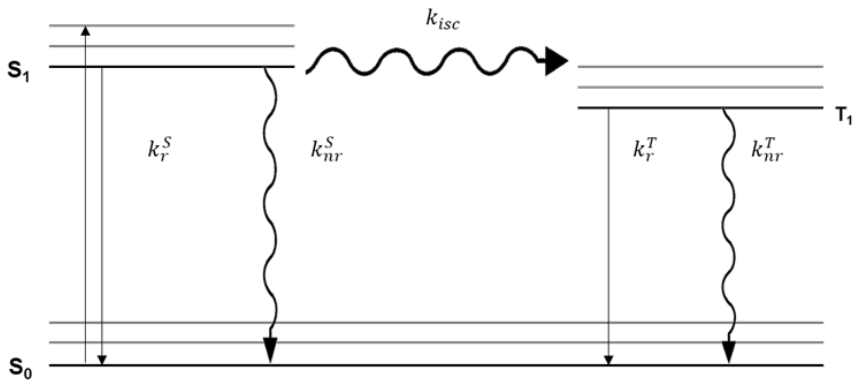

Figure 2.4 - Jablonski diagram and kinetic constants of decays. Radiative kinetic constants are presented with the r subscript, and non-radiative processes with nr.

The Jablonski diagram represents the fate of the excited states. Hund's rule states that two electrons placed in distinct orbitals with parallel spin configuration, have an energetic favourable configuration than a paired spin configuration. For this reason energy of the triplet state is smaller than the energy of the singlet excited state. Singlet or triplet states light emission cover an important energy region whose efficiency describes the amount of photons that intervene in the photophysical process. Quantum efficiency, or quantum yield, (ϕ_L), is defined as the fraction of photons emitted per photons absorbed.

$$\phi_L = \frac{number\ of\ photon\ emitted\ (per\ time\ per\ volume)}{number\ of\ photon\ absorbed\ (per\ time\ per\ volume)} \quad (5)$$

2.3.1. Tin and copper oxide photoluminescence

Tin is a post-transition metal, the fourth member of the group 14 of the periodic table. The same group which accommodates carbon, silicon, germanium and lead. Tin has an electronic configuration of [Kr] $4d^{10}$ $5s^2$ $5p^2$, with two main oxidation states, stannous Sn^{2+} and stannic Sn^{4+}. Tin oxide (SnO_2) is a semi-conductor material with a wide and direct band gap of 3.6 eV which makes it an excellent candidate for large band energy conversion[34]. Regarding its photoluminescent behaviour in glass, it has been reported that tin oxide doped glasses exhibit light emission via the absorption of UV light[10]. Tin oxide has an ns^2-type emissive center (with $n \geq 4$), common to Sb^{3+}, Hg^0, Tl^+, and Pb^{2+} which exhibit photoluminescence derived from the the parity allowed transition from the singlet ground state $5s^1$ $5p^1 \rightarrow$ $5s^2$, and from the partially forbidden transition between singlet state and the first excited triplet state $5s^1$ $5d^1 \rightarrow 5s^2$ [13].

Copper is a transition metal the first member of group 11 of the periodic table, the same group which accommodates silver and gold. With an electronic configuration of [Ar] $3d^{10}$ $4s^1$, copper has two common oxidation states, cuprous ion Cu^+ and cupric ion Cu^{2+} [35]. Cu_2O is a conductive material with a direct band gap of 2.1 eV [34]. Its photoluminescent behaviour in glass has shown visible light

emission derived from UV light absorption through the allowed transition between singlet states $3d^{10} \rightarrow 3d^9$ 4p and the partially forbidden triplet transition $3d^{10} \rightarrow 3d^9 4s$ [36].

2.4. *Thin Film sputtering*

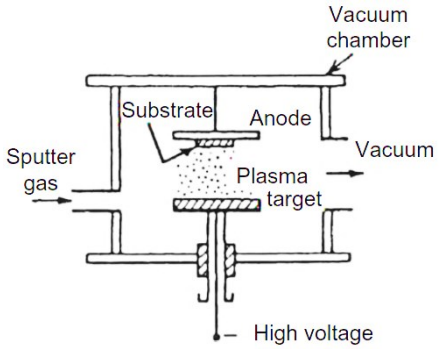

Figure 2.5 - Radio-frequency magnetron sputtering simplified scheme.

Preliminary studies regarding copper and tin thin film deposition will also be approached. A common fabrication method for thin films is the radio-frequency magnetron sputtering (rRF-MS) a physical vapour deposition (PVD) technique extremely capable of fast and precise control over deposition process parameters on large areas.

Sputtering describes the deposition technique in which positively ionized particles of sufficient kinetic energy are used to sputter material from a solid target without the need of heat. The creation of these positive ions depend on the formation of a plasma induced by a strong electric field, applied between a target (cathode) and a substrate (anode), and the introduction of an inert noble gas species (commonly argon). In order to create a plasma a vacuum chamber is also required, where a high vacuum base pressure must be reached before the deposition process. When an efficient process is developed it enables a controlled particle transfer from a target source onto a solid substrate where a thin film is formed.

The oxidation state of the deposited film can be modified through the introduction of reactive gas species to the process; the reactive gas may induce a chemical reaction in the plasma altering the composition of the deposited film. The reactive gas also becomes partially ionized by the plasma, and the ejected metal particles react either with charged or neutral ions. Partial pressure control over the ratio of volumetric reactive component gas flow rate is a key factor to induce the desired stoichiometry of the final compound [26].

With the objective of developing photoluminescent thin-films through usage of tin and copper oxides, preliminary studies will be attempted in order to characterize the oxide formation due to variable oxygen flow. Afterwards, thermal treatment will be applied to the samples in order to evaluate possible copper and tin diffusion into the glass substrate.

2.5. *Luminescent solar concentrator*

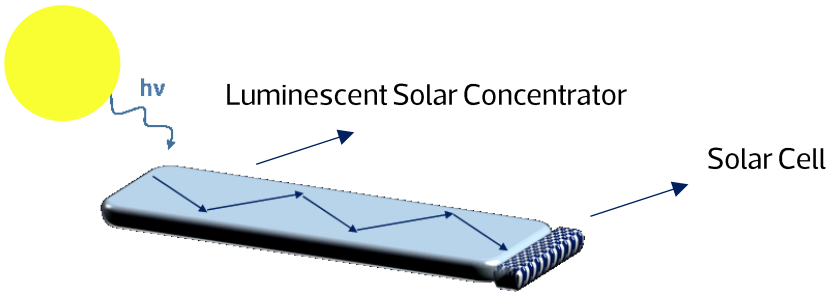

Figure 2.6 - Schematic example of the waveguide function of a luminescent solar concentrator.

Samples produced during this study are expected to behave as luminescent solar concentrators (LSC), specific devices able to down-convert solar harvested energy. The doped glass behaves as an insulator and it is able to harvest and concentrate energy in its interior. Through the internal reflection of the glass matrix a waveguide function arises, directing light towards a specific geometrically dependent location where it may be converted into electricity by photovoltaic (PV) cells installed along the edges of the material. Efficiency of this process is of major relevance to the development of PV cells since high energy photons are not as efficiently absorbed by PV cells as low energy photons[5].

A LSC has the potential of integration use in photovoltaics who require high quantum efficiencies and large Stokes shifts, both are necessary features for efficient UV light conversion and suppressing light reabsorption in large-area devices. Despite the huge promise, the use of LSCs has been slow due to absence of suitable light emitters, the commonly used organic chromophores are necessarily applied in polymers whose estimated lifetime is of 25 years when subject to constant solar radiation and atmospheric conditions[54]. The extreme durability of glass present an opportunity to develop highly stable and efficient semi-transparent photovoltaic windows fundamental for the net zero energy consumption buildings of the future[5].

3. Tin doped alumina-borosilicate glass

The introduction of tin oxide to a glass matrix has been performed [10-13], to the best of our knowledge no systematic variation in concentration amounts of doping was found. From this study we intend to determine an optimum amount of doping which determines the highest quantum efficiency. Such objective is intended to ascribe the optimized properties of these samples in order to evaluate the individual behaviour of the elements, and possible photoluminescence interaction between tin and copper oxide.

3.1. *Synthetic procedure*

Taking into account the synthetic strategy presented in the selected work[16], a similar approach was adopted. The same set of elements were used in order to obtain a multicomponent alumina-borosilicate glass, however barium oxide was removed as well as the luminescent element lead oxide. With the purpose of maintain the structural features of the matrix, batch preparation was accomplished through maintenance of the molar ratio between B_2O_3/SiO_2 = 0.256; Al_2O_3/SiO_2 = 0.099, AlkaliOxide/SiO_2= 0.156, and SnO/SiO_2=0.021. Seven samples were produced by variation of the amount of tin, whose composition can be consulted in table 3.1. Sample names are expressed in mol % Sn during the text.

Table 3.1 - Nominal composition of samples, in molar percentage, of tin doped alumina-borosilicate glasses, BG stands for base glass, Tin sample number (Tx).

Sample	SiO_2	B_2O_3	Al_2O_3	SnO	Li_2O	Na_2O	K_2O
BG	66.2	16.9	6.6	0.0	5.7	3.6	1.1
T1	65.9	16.9	6.5	0.4	5.6	3.6	1.1
T2	65.7	16.8	6.5	0.7	5.6	3.5	1.1
T3	65.4	16.7	6.5	1.1	5.6	3.5	1.1
T4	65.3	16.7	6.5	1.4	5.6	3.5	1.1
T5	64.4	16.5	6.4	2.8	5.5	3.5	1.1
T6	63.9	16.3	6.3	3.4	5.5	3.4	1.1

The following chemical reagents were used as starting materials, purity grade is described as follows: SiO_2 (p.a., Sigma-Aldrich), B_2O_3 (99%, AlfaAesar), Al_2O_3 (p.a., Fluka Analytical), Li_2CO_3 (98%, Fluka Analytical), Na_2CO_3 (99.5%, Panreac), K_2CO_3 (99%, Sigma-Aldrich), and SnO (99%, AlfaAesar).

Approximately 50g batches were mixed in a shaker powder mixer for one hour (Turbula T2F), and melted in a platinum crucible. An electrical furnace was used for melting at 1400 ºC for 2.50 hours, at regular atmosphere. The melt was quenched onto a metal sheet at room temperature, and annealed at a temperature of 540 ºC for one hour. Glass samples were cut and polished, approximately 6 mm thick, for optical and Raman measurements. For dilatometry analysis, samples were prepared with approximately 2.5 cm wide and 5 mm diameter. For solid state NMR (SSNMR),

samples were crushed for 15 min in a ball mill at 500 rpm and sieved for ≤120 μm particles. Sample analysis was performed through several techniques whose conditions may be accessed in supplementary information.

3.2. *Results and discussion*

Glasses samples obtained are completely transparent, the increase of tin oxide concentration shown an increase in melt viscosity which characterized a difficult sample quenching procedure. It is possible to observe trapped gas on the samples interior. In figure 3.1 all tin oxide doped samples were photographed under a 5.16 eV UV lamp light showing the luminescent Sn^{2+} light emission, through a characteristic white-blue light.

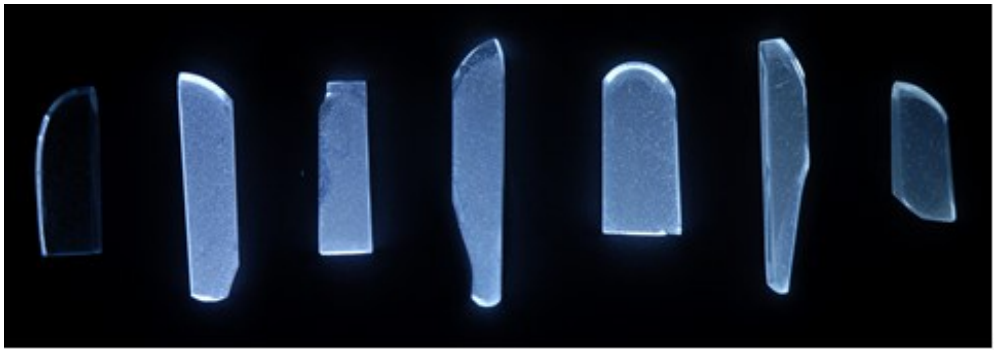

Figure 3.1 - Tin oxide doped samples under 5.16 eV excitation wavelength, from left to right: BG-0%Sn, T1-0.4%Sn, T2-0.7%Sn, T3-1.1%Sn,T4-1.4%Sn, T5-2.7%Sn, T6-3.4%Sn.

3.2.1. Solid state nuclear magnetic resonance (SSNMR)

To evaluate tin oxide doping interference with the global structure of the glass SSNMR was performed using single pulse magic angle spinning (MAS) technique, where ^{29}Si (spin -1/2 nuclei) was studied. Spectra (figure 3.2) shows the presence of a convolution of at least 2 distinct peaks, a feature which becomes evident with tin oxide doping, a broad Gaussian peak, at -102 ppm, which

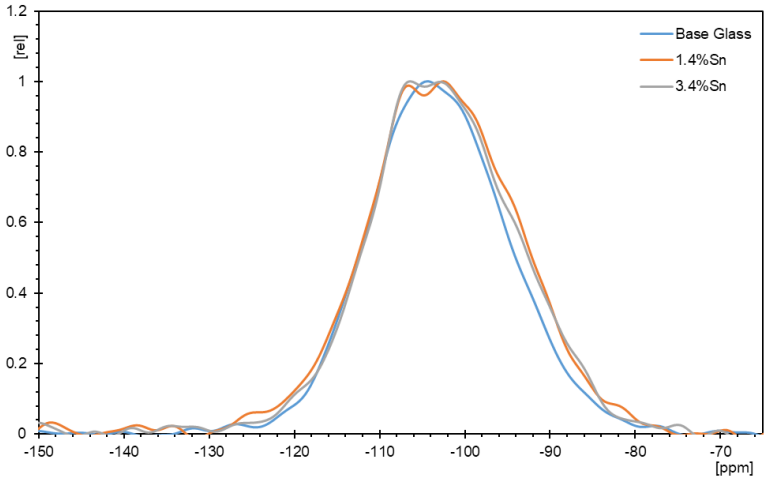

Figure 3.2 - Single pulse MAS technique, ^{29}Si (spin - 1⁄2 nuclei) normalized spectra, study was performed over the base glass, 1.4% Sn and 3.4% Sn.

is due to the ^{29}Si present in the glass framework[37] and a sharp peak, at -107 ppm , due to the ^{29}Si presence in crystalline quartz[38]. Spectra for all samples present consistency, suggesting that doping is not inducing variation of the silicate structure. We have also attempted to study ^{119}Sn (spin -1/2 nuclei), however the small molar percentage of tin oxide doping in addition to the small isotope percentage (8.6%) of ^{119}Sn made this study impossible.

3.2.2. Raman spectroscopy

Raman spectroscopy was performed on three samples, base glass, 1.4%Sn and 3.4%Sn, figure 3.3. A high degree of similarity is found between the spectra of these samples, although some variation is introduced with tin oxide doping, specifically a distinct peak at ~350 cm^{-1} which is inhibited and shape change from 850-1250 cm^{-1}.

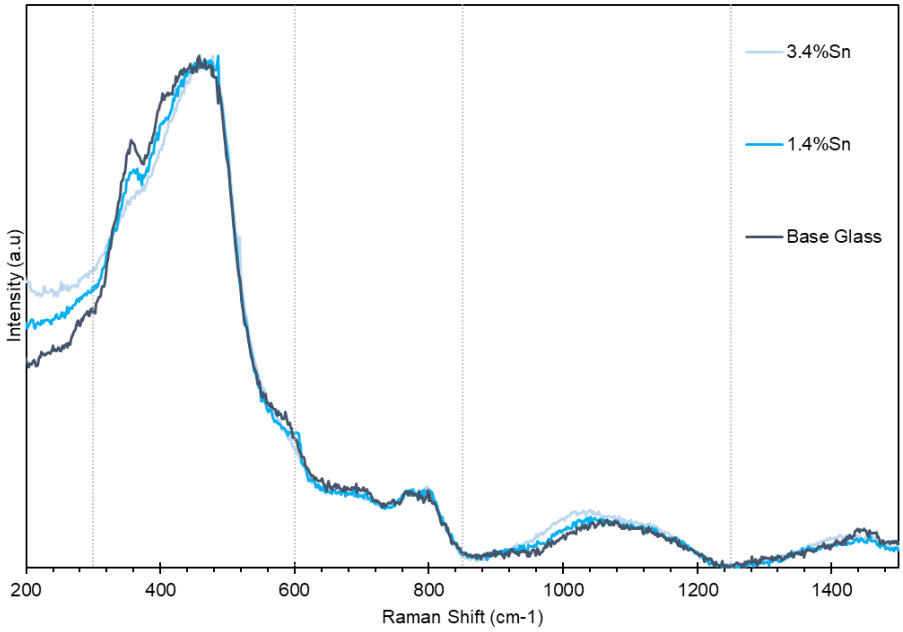

Figure 3.3 – Raman Spectra for Base Glass (BG), 1.4% Sn and 3.4% Sn.

The first region of interest, the 300-500 cm^{-1} window, has been associated to the overall connectivity of the silica network, specifically regarding stretching or bending modes of Si−O−Si bonds and also to the extent of polymerization of the borosilicate network [16]. Mixed modes related to bending or rocking vibrations of the network borosilicate linkage can also be identified through the medium-range vibrational modes, from 400 to 850 cm^{-1}, associated to the formation of ordered superstructures reedmergnerite $[BSi_3O_8]^-$ and danburite $[B_2Si_2O_8]^{2-}$ [39]. It is observable for all samples that a peak located at ~800 cm^{-1} is persistent both in shape and position. The concerning region has been associated with the boron network, where Raman modes have been assigned to the formation of triborate, tetraborate or pentaborate groups, through splitting of boroxol ring oxygens (800 cm^{-1}) (B_3O_6, appendix, figure 8.6) in the presence of a suitable modifier ion[40].

Characteristic Raman bands in the high frequency interval of 850-1250 cm^{-1} are associated with the asymmetric vibration of SiOx structures, specifically related to Q_2^{Si} at 850 and 950 cm^{-1}, Q_3^{Si} at 1000, 1050 and 1080 cm^{-1}, and Q_4^{Si} at 1150 cm^{-1} [40]. Q^{Si} represents the silicate tetrahedral unit and Q_n represents the number of bridging oxygens (BO) per tetrahedron. The observation of a broad

band suggests that coupling between these mixed modes of vibration may exist, therefore Raman spectra deconvolution was performed for the analysed samples. (See appendix: Figure 8.1) Three gaussian (equation 6) bands correspondent to the structural evolution of $\boldsymbol{Q_2^{Si}}, \boldsymbol{Q_3^{Si}}, \boldsymbol{Q_4^{Si}}$ units with tin oxide doping were identified. Results are constant, only varying when tin concentration is 3.4% Sn, through a 5% increase of area value for Q_4^{Si} structural units in detriment of $\boldsymbol{Q_3^{Si}}$ units, while $\boldsymbol{Q_2^{Si}}$ structural units are reduced by a 0.5% value.

$$F(x) = \frac{1}{\sqrt{2\pi\sigma^2}} \times e^{\frac{-(x-\mu)^2}{2\sigma^2}} \quad (6)$$

Table 3.2 - Raman shift of $\boldsymbol{Q_2^{Si}}, \boldsymbol{Q_3^{Si}}, \boldsymbol{Q_4^{Si}}$ structural units obtained in the deconvolution of Raman spectra in the 850-1250 cm^{-1} region for tin oxide doped samples.

		$\boldsymbol{Q_2^{Si}}$	$\boldsymbol{Q_3^{Si}}$	$\boldsymbol{Q_4^{Si}}$
Base Glass	σ (cm^{-1})	20.3	55.5	41.4
	μ (cm^{-1})	915.5	1054.7	1151.9
	A%	3.2	69.4	27.4
1.4% Sn	σ (cm^{-1})	19.4	57.8	41.3
	μ (cm^{-1})	918.7	1044.1	1150.3
	A%	3.2	69.3	27.6
3.4% Sn	σ (cm^{-1})	20.6	54.7	44.7
	μ (cm^{-1})	921.9	1027.4	1138.6
	A%	2.6	64.1	33.3

3.2.3. Dilatometry

The thermomechanical behaviour of glass is directly correlated to the density and organization of the structural matrix, where elasticity and viscosity are directly affected. The use of dilatometry technique permits to obtain three parameters that characterize glass thermomechanical properties (see representation in appendix, figure 9.1):

1. The coefficient of thermal expansion (CTE) represents the temperature dependent expansion ability of a material, it is mathematically represented through value of the slope of the first linear interval of the thermal expansion data;

2. The glass transition temperature (T_g) indicates value for the glass phase transition of a material, it is determined through the intersection of the linear expansion phase transition data;

3. The softening temperature (T_s) is the temperature at which glass viscosity reaches a limit value where the material is still capable to prevent deformation due to its own weight. Its value is determined from the maximum value of the data.

Thermal expansion coefficient analysis show that base glass CTE value is increased with tin oxide doping. Sample 0.7% Sn onward shows a decreasing trend of the value. The working temperature variation is apparently stable throughout the doping procedure. These values are slightly higher than a common borosilicate glass (pyrex), $3.3x10^{-6}$ K^{-1}, but lower than a soda lime glass $8.6x10^{-6}$ K^{-1}.

Table 3.3 - Dilatometry analysis results for tin oxide doped samples. Glass Transition Temperature (T_g), Softening temperature (T_s), and Coefficient of Thermal Expansion (CTE).

Sample	CTE $_{25\text{-}350^oC}$ $*10^{-6}$ (K^{-1})	T_g (ºC)	T_s (ºC)
BG	6.58	478.8	537.3
0.35% Sn	6.82	482.7	542.3
0.7% Sn	7.29	486.0	540.0
1.1% Sn	7.0	477.3	530.6
1.4% Sn	6.18	471.3	539.8
2.7% Sn	6.49	467.8	534.7
3.4% Sn	6.03	470.0	533.1

Glass transition temperature increases with the addition of tin oxide, however for concentrations larger than 0.7% Sn T_g values decrease trending to a value of ~470 ºC. These values show that there is no significant variation of temperature from the doping procedure. These values are considerably lower than common pyrex glass transition temperature, 560 ºC.

Results for the softening temperature (T_s) show that small amount of doping originate a 5º C increase of the softening temperature, while further doping follows a decreasing trend, with a lower value than the base glass, and significantly lower than the extremely resistant pyrex glass, 820 ºC.

3.2.4. UV/Vis Spectroscopy

The optical transmittance spectra obtained for Sn doped samples is shown with the base glass as reference, figure 3.4. A characteristic UV-cut off edge is represented for all samples. The importance of the cut-off value resides in determining the inherent capacity of a glass matrix to absorb light. Its values wil interfere with the doping species absorbing ability affecting the samples quantum efficiency. Cut-off values can be obtained by extrapolation of the linear segment of the transmittance edge, forcing the ordinate value to zero. Table 3.4 shows the obtained values, reflecting the bathochromic variation of the cut-off edge due to tin oxide doping.

Table 3.4 - Optical cut-off values for tin oxide sample glasses, values in eV.

Sample	BG	0.35% Sn	0.7% Sn	1.1% Sn	1.4% Sn	2.7% Sn	3.4% Sn
Cutoff (eV)	4.03	3.96	3.91	3.88	3.82	3.70	3.65

Variations in the optical absorption edge can be dependent on the glass network change effect induced by SnO addition or substitution of Si atoms in the coordinated matrix, being directly related to the deep-UV light absorption from heterogeneous tin oxide structures, possibly aggregates of two or three fold coordinated tin oxide centres[41][42]. The observed values reflect a high degree of transparency, take in mind that pure quartz cuvettes used for spectroscopic analysis have a UV cut-off edge of 6.1eV.

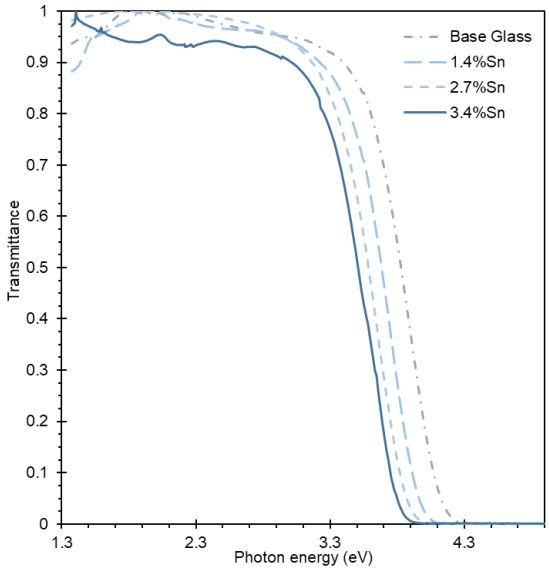

Figure 3.4 – Normalized optical transmittance spectra of tin doped samples with base glass as reference.

3.2.5. Excitation Spectroscopy

Photoluminescent excitation spectra profile (figure 3.5) was performed by monitoring light emission at 3.5 eV. Two excitation bands are observable as dominant spectral features, for each sample we find a high energy band at 5 eV and a lower energy band located at approximately 4.3 eV. A gradual intensity growth is shown for small doping concentrations, for sample 1.1% Sn and larger concentrations excitation intensity is inhibited, with the low energy maximum suffering a slight red-shift trend. The amount of doping in the samples shows a similar excitation profile for the samples. The low energy band, associated with the triplet emission of tin oxide, shows a more intense nature than the high energy band, correspondent to the singlet emission, such is due to its

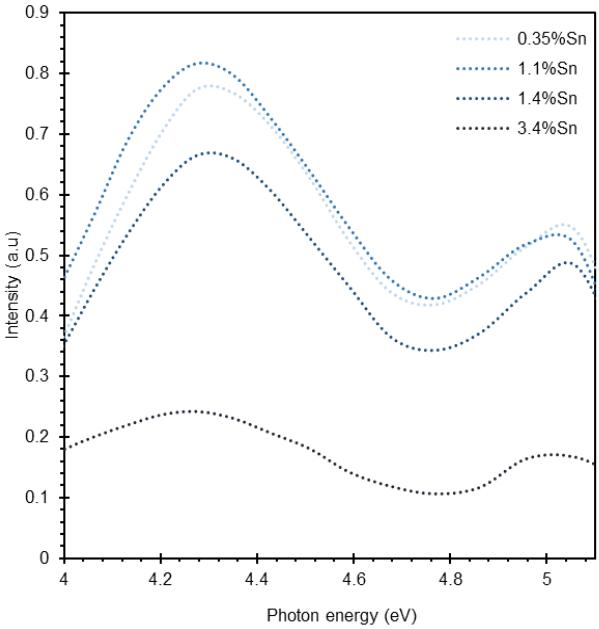

Figure 3.5 - PLE spectra of tin doped samples, light emission monitored at 3.4 eV.

proximity to the cut-off region, enabling a more efficient light absorption through this radiative channel.

3.2.6. Emission spectroscopy

Emission spectra is shown in figure 3.6, it was obtained through sample excitation at 4.2 and 4 eV. The emissive spectra shows a broad light emission which surpass the analysis limits, this is related to heterogeneous formation of tin oxide emissive centres. Figure 3.6 (a) show a constant high energy emissive peak at 3.8 eV which derives from the triplet state emission. A second emissive low energy band is seen to arise for concentrations larger than 1.4 % Sn. This low energy band redshifts with doping, from 2.8 to 2.5 eV surpassing the intensity of the high energy band for sample 2.7% Sn, becoming the dominant emissive maximum. These observations suggest the existence of two major emissive species whose emissive behaviour is dependent on doping concentration. Similar features are also observed with sample excitation at 4 eV, concentration quenching of the first emissive maximum is observed, and also the emissive maximum is progressively redshifted with doping, from 3.5 eV to 2.5 eV. Tin oxide doping determines as a general trend spectral broadening and red-shifting of the low energy emissive peak.

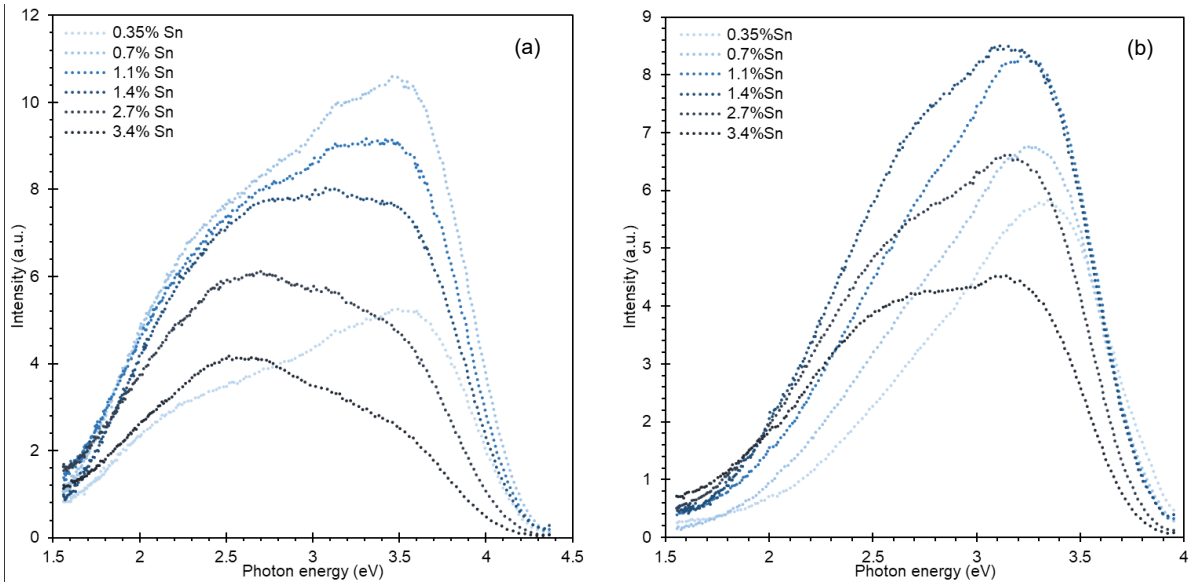

Figure 3.6 - PL spectra for the batch of tin samples excited at (a) 4.4 eV and (b) 4 eV.

3.2.7. Photoluminescence Kinetic Decay

Electronic nature of the Sn^{2+} luminescent centres was evaluated through its photoluminescence kinetic decay, figure 3.7. Through excitation at 3.5 eV and light emission monitoring at 3.2 eV, results show a bi-exponential profile with slight variation of the short component decay time ~9.8 μs, and of the longer component decay time 16.8, 17.2 and 17.6 μs, for samples 0.7%, 1.4% and 3.4% Sn respectively.

Table 3.5 - Photoluminescence kinetics decay time for tin oxide doped samples (μs).

	0.7% Sn	1.4% Sn	3.4% Sn
τ_1	9.76	9.84	9.84
τ_2	16.85	17.18	17.58

The observed long lifetime values of the two emissions suggest that both are triplet states, the shorter time values are in good agreement with what literature reports for the triplet transition of a Sn^{2+} luminescent centre in glass, 11 μs [13].The origin of the larger decay time can be rationalized through the formation of tin oxide aggregates where the bonding interaction of the empty 5p atomic orbitals of tin oxide originates orbital splitting into two emissive triplet states, a faster less energetic state and a slower more energetic state.

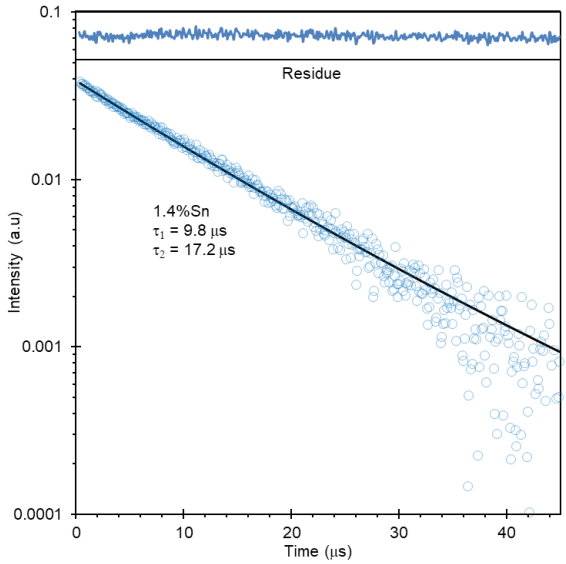

Figure 3.7 - Photoluminescence kinetic decay fit for sample 1.4%Sn, excitation at 3.5 eV, emission monitored at 3.18 eV.

3.2.8. Quantum yields

Luminescent quantum yields (Φ_L) were obtained from the absolute emission method, with samples being measured at different excitation energies, at 4.1 eV, 3.8 eV and at 3.4 eV. Figure 3.8. show that quantum yields are higher for excitation at 4.1 eV, at this energy value we are near the cut-off region, which enables a more efficient light absorption process. A clear pattern is observed from the doping results, quantum efficiency is higher for intermediate concentrations of tin oxide, specifically for samples 0.7% Sn, 1.1% Sn and 1.4% Sn which show 48% efficient photon conversion. Larger doping concentrations show a decrease tendency of quantum efficiency, reflecting how larger doping amounts increase the non-radiative constant of the photophysical pathway.

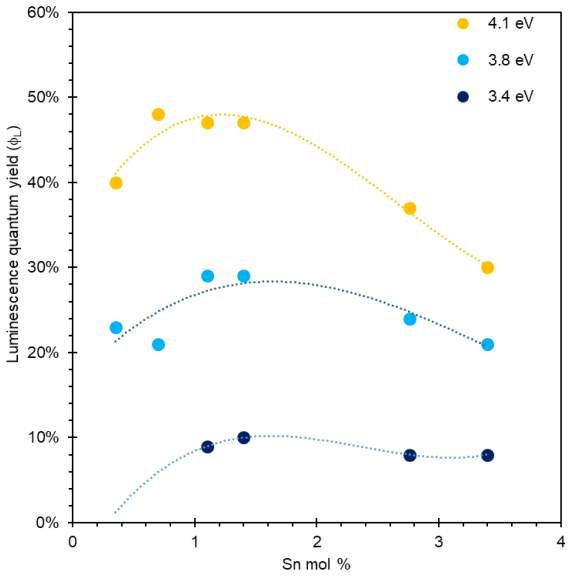

Figure 3.8 - Luminescence quantum yields of tin doped samples, excitation at 4.13, 3.76 and 3.44 eV.

3.3. *Conclusions*

The obtained tin oxide doped samples show white-blue emissive light under all concentrations (figure 3.9). Solid state NMR analysis revealed that no structural change was induced by doping the silicate network. This observation is corroborated with Raman spectroscopy which revealed that doping had a low impact over the silicate structure, with for Q_4^{Si} structural units being increased by 5% with doping, in detriment of $\boldsymbol{Q_3^{Si}}$ units, while $\boldsymbol{Q_2^{Si}}$ structural units are reduced by a 0.5% value.

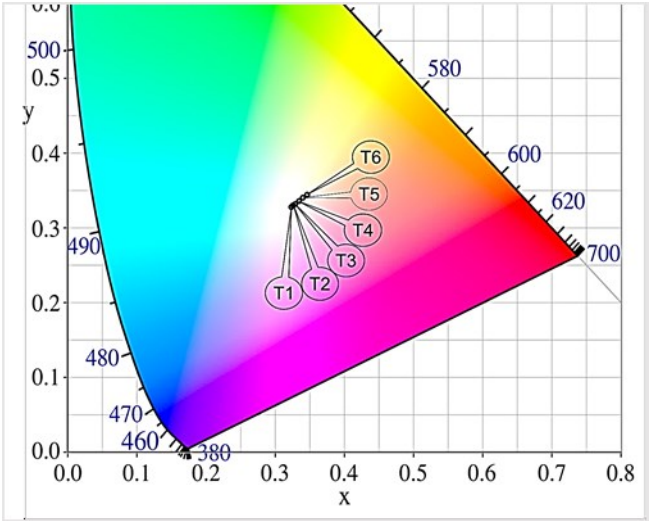

Figure 3.9 - Colour coordinates of tin doped samples, excitation at 4.4 eV.

Further information was revealed regarding the development of interaction between both primary structural networks, two ordered macrostructures reedmergnerite $[BSi_3O_8]^-$ and danburite $[B_2Si_2O_8]^{2-}$ were formed, and also the formation of boroxol rings and associated structures are features which are not dependent on doping.

Samples thermomechanical properties reveal that glass transition temperature, melting temperature or thermal expansion coefficient results present a small degree of variance with tin oxide doping, with no particular trend being observed.

UV/Vis light absorption show how doping induces a UV cut-off edge bathochromic shift, while the host glass cut-off edge is located at 4 eV for the host glass, 3.4% Sn sample shows a 3.65 eV value for the cut-off edge. Taking into account the two excitation sites identified for the samples, the high energy peak responds to excitation in the deep-UV at 5 eV, and the low energy band is found at lower energies, 4.3 eV, a significant part of UV light absorption is accomplished through the host matrix.

Variation of Sn^{2+} doping concentration clearly shows the development of heterogeneous emissive centres, which result in a characteristic broad light emission spectrum, from 5 eV to 1.4 eV, notorious for all concentrations. The new emissive maximum formed with high doping concentration is a solid evidence of the heterogeneous formation of luminescent tin oxide centres.

Two distinct emissive species were identified, the kinetic decay profile was adjusted through a bi-exponential expression with a faster constant value of 9.8 μs, associated with the emission of tin oxide, and slight variation of the slower component with an average value of 17 μs associated with the formation of tin oxide dimers. The nature of these values indicate we are observing partially forbidden transitions correspondent to triplet to singlet electronic states.

Both excitation bands show light emission at approximately 3.5 eV, which represent a large Stokes shift of 1.7 eV for the high energy excitation band and a smaller 0.8 eV Stokes shift for the low energy excitation band. This means that we have a negligible overlap between the absorption and emission profiles, inhibiting the reabsorption capability of Sn^{2+} luminescent centres.

Quantum efficiency reached a peak value of 48% for intermediate tin oxide concentration, 0.7% Sn, 1.1% Sn and 1.4% Sn, revealing the luminescence quenching effect induced through the formation of tin oxide aggregates, reflecting the increase of the non-radiative constant for sample concentrations larger than 1.4% Sn.

Taking into account the obtained results, the observed photoluminescent pathways may be schematically represented as in figure 3.10.

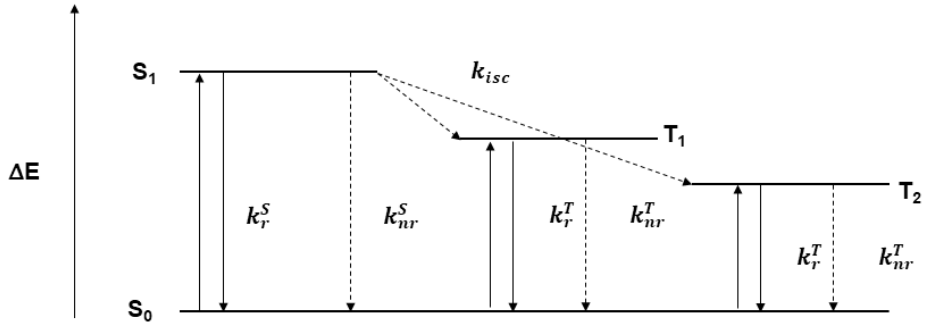

Figure 3.10 - Proposed scheme of electronic levels and related radiative (full-line) and non-radiative (dashed line) processes accounted for the analysis of PL emission of Sn doped samples.

4. Tin and Copper oxide doped alumina-borosilicate glass

Introduction of both tin and copper oxide into the glass structure has a subjacent interest to the study which is to evaluate if any structural or photoluminescent interaction between both species occurs. With this purpose, tin oxide will be inserted with a fixed concentration of 1.4%, an amount which is sufficient to fully reduce Cu_2O, while also showing to induce no change to the matrix structure and presented the maximum value of quantum efficiency.

4.1. *Synthetic procedure*

To optimize the synthetic procedure, especially to guarantee sample homogenization, melting temperature was increased from 1400 º C to 1550 ºC since at higher temperature viscosity of the melt is reduced, such enables a more effective dispersion of the elements in the matrix and an optimized glass structure. Mechanical homogenization procedures were also performed to the melt with swirling and crushing of the glass being performed during the melt procedure for each sample. Taking into account the T_g values obtained for tin oxide doped samples, and in order to reduce ionic mobility over the thermal treatment procedure, the annealing temperature was decreased, from 540º C to 420 ºC.

Batch preparation was accomplished as previously reported, the ratio between elements was maintained B_2O_3/SiO_2 = 0.256; Al_2O_3/SiO_2 = 0.099 and AlkaliOxide/SiO_2= 0.156, with variation of the amount of CuO between [0-0.14] % mol. An undoped glass sample was produced as well as a tin oxide doped (1.4% Sn) sample for reference purposes, adding to a total of 7 samples produced. Sample names are expressed in mol % Cu during the text.

Table 4.1 - Nominal composition of samples, in molar percentage, of tin and copper doped alumina-borosilicate glasses, BG stands for base glass, Copper sample number (Cx).

Sample	SiO_2	B_2O_3	Al_2O_3	SnO	Li_2O	Na_2O	K_2O	CuO
BG	66.2	16.9	6.6	0.0	5.7	3.6	1.1	0.00
C1	65.3	16.7	6.5	1.4	5.6	3.5	1.1	0.00
C2	65.2	16.7	6.5	1.4	5.6	3.5	1.1	0.01
C3	65.2	16.7	6.5	1.4	5.6	3.5	1.1	0.03
C4	65.2	16.7	6.5	1.4	5.6	3.5	1.1	0.05
C5	65.1	16.6	6.5	1.4	5.6	3.5	1.1	0.08
C6	64.9	16.6	6.4	1.4	5.6	3.5	1.1	0.14

Batch materials were reagent grade. Their origin and purity grade are described as follows: SiO_2 (p.a., Sigma-Aldrich), B_2O_3 (99%, AlfaAesar), Al_2O_3 (p.a., Fluka Analytical), Li_2CO_3 (98%, Fluka Analytical), Na_2CO_3 (99.5%, Panreac), K_2CO_3 (99%, Sigma-Aldrich), and SnO (99%, AlfaAesar).

Approximately 50 g batches were mixed in a shaker powder mixer for one hour (Turbula T2F), and melted in an electrical furnace at 1550 ºC for 2.50 hours, in a platinum crucible at regular atmosphere. Each sample was stirred, cooled and crushed manually for 3 times after 30, 60 and 90

minutes of melting. The melt was quenched onto a metal sheet at room temperature, and annealed at a temperature of 420 ºC for one hour. Glass samples were cut and polished, with approximately 1 cm wide and 0.6 cm thick, for optical and Raman measurements. For dilatometry analysis samples were prepared with approximately 2.5 cm wide and a diameter of 5 mm. For SSNMR and XRD samples were crushed for 15 min in a ball mill at 500 rpm and sieved for ≤120 μm particles. Sample analysis was performed through several techniques whose conditions may be accessed in supplementary information.

4.2. *Results and discussion*

Figure 4.1 shows the obtained samples under a 3.4 eV UV light. Glass samples are transparent and it is possible to observe trapped gas on the inside. Melt viscosity was evidently reduced with all samples showing great fluidity for quenching. A three colour gradient was obtained, tin oxide doping showed its blue emissive colour, small addition of copper induces a blue-white tone while larger amounts of copper doping originate a yellow light emission.

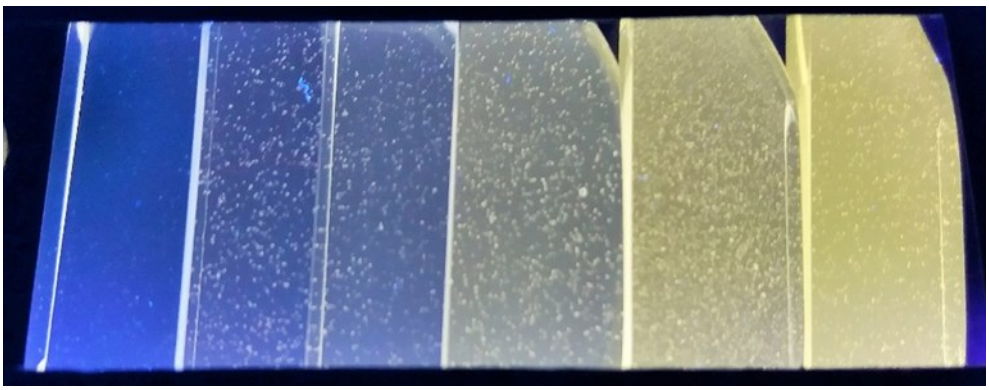

Figure 4.1 - Tin and copper oxide doped samples melted at 1550 ºC light emission when excited at 3.4 eV. From left to right: C1 - 0% Cu, C2 - 0.01% Cu, C3 - 0.03% Cu, C4 - 0.05% Cu, C5 - 0.08% Cu, C6 - 0.14% Cu, (%mol).

4.2.1.X Ray-Diffraction (XRD)

Structural change of the host matrix was evaluated through XRD, figure 4.2 shows the normalized spectra of the samples. Copper doped glass samples show the characteristic amorphous profile of glass which can be identified through a broad peak at 22º 2θ. The presence of crystalline peaks are also found at 20.7º 2θ and 26.8º 2θ which are related to residual formation of quartz [43].

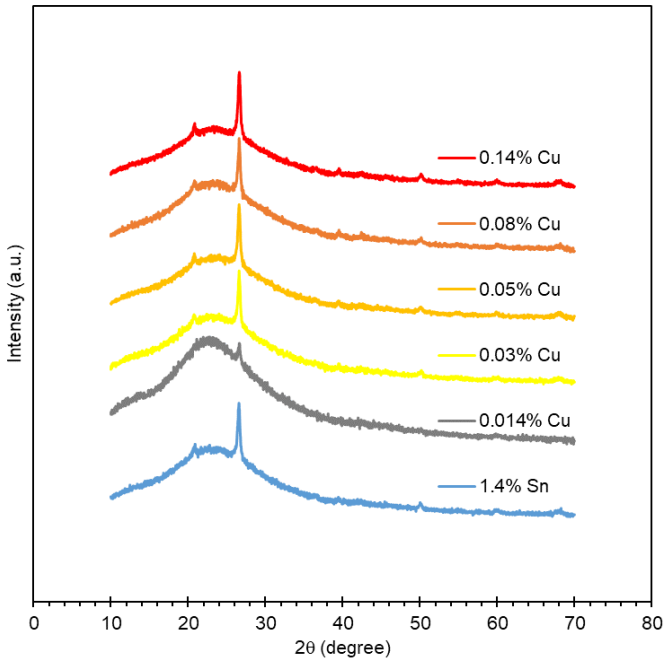

Figure 4.2 - X-Ray diffraction spectra of copper and tin doped samples at 1550 ºC.

4.2.2. SS NMR

Solid-state NMR was used to probe the local environment and coordination mode of a range of nuclei, including ^{29}Si (spin-1⁄2 nuclei), ^{11}B, ^{27}Al, and ^{23}Na (quadrupolar nuclei, with spin 5/2, 3/2 and 3/2 respectively). The ^{29}Si spectra, figure 4.3, shows two 2 coincident peaks: a broad Gaussian peak, at -102 ppm, due to the ^{29}Si present in the glass framework[37]; and a sharp peak, at -107 ppm, associated with ^{29}Si formation of crystalline quartz[38].

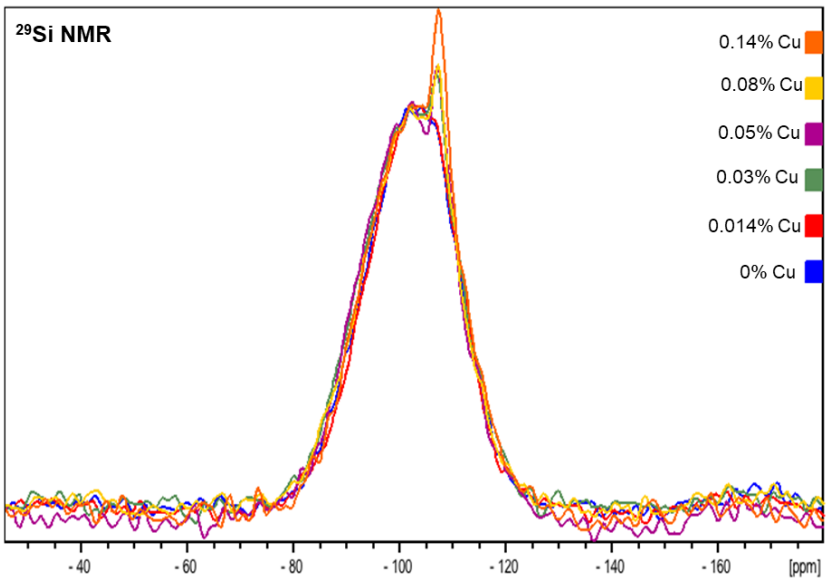

Figure 4.3 - ^{29}Si NMR spectra for whole batch of copper doped samples

The ^{11}B spectra (figure 4.4) shows two peaks at 12 ppm and 0 ppm for single-pulse and Hahn-echo experiment, respectively. The peak at 0 ppm is originated from tetra coordinated boron, BO_4, while the peak at 12 ppm is associated with tri-coordinated boron, BO_3. The relative intensity of these peaks seems to change from sample to sample, but no obvious trend is found[57].

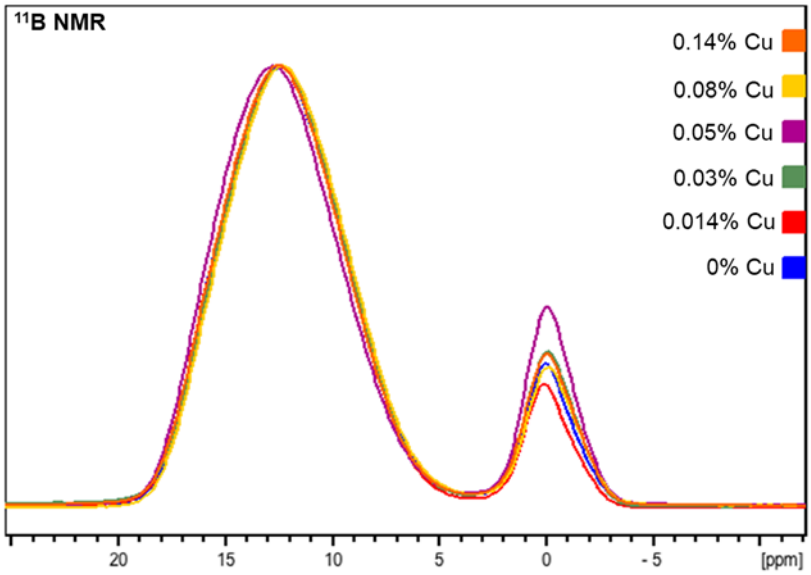

Figure 4.4 - ^{11}B NMR spectra for whole batch of copper doped samples.

The ^{23}Na spectra (figure 4.5) showed a single broad peak at -15 ppm. This value for the chemical shift of ^{23}Na is associated with non-bridging oxygen atoms in the structure and the sodium acting as charge compensator, it is a characteristic peak which demonstrates sodium's modifier role in the glass matrix. For sample 0.05% Cu, a clear hump at -6 ppm is observed, associated with the formation of $NaAlSi_3O_8$.[44].

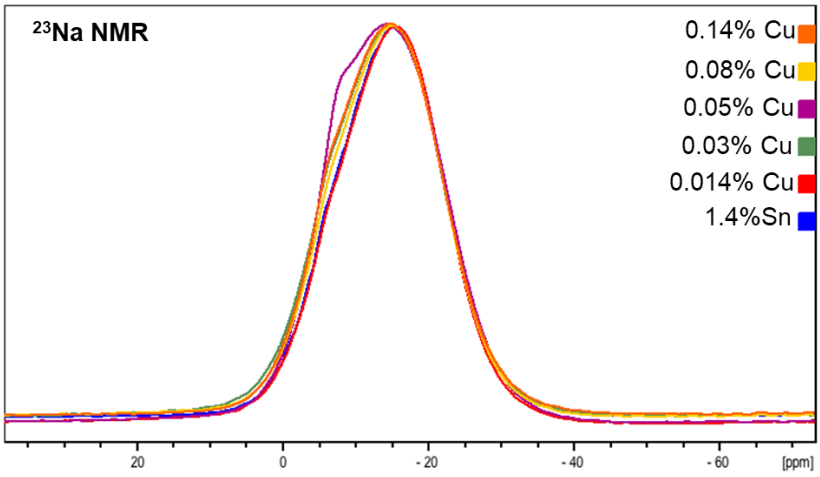

Figure 4.5 - ^{23}Na NMR spectra for whole batch of copper doped samples.

We have also attempted to study ^{119}Sn (spin -1/2 nuclei). However the small molar percentage of tin oxide doping in addition to the small isotope percentage (8.6%) of ^{119}Sn made this study impossible.

4.2.3.Raman spectroscopy

Raman spectroscopy was performed on base glass, 1.4% Sn, 0.014% Cu, 0.05% Cu and 0.14% Cu, figure 4.6. The general structure of the spectra is similar with tin oxide doped samples analysed. From 300-500 cm^{-1} the overall connectivity of the silica network is analysed, specifically regarding stretching or bending modes of Si−O−Si bonds, being also related to the extent of polymerization of the borosilicate network[16]. The left shoulder at 350 cm^{-1} shows intensity fluctuation due to tin and copper oxide doping. Intensity of this peak is reduced with tin oxide and increased for higher copper concentrations but no definite trend can be identified.

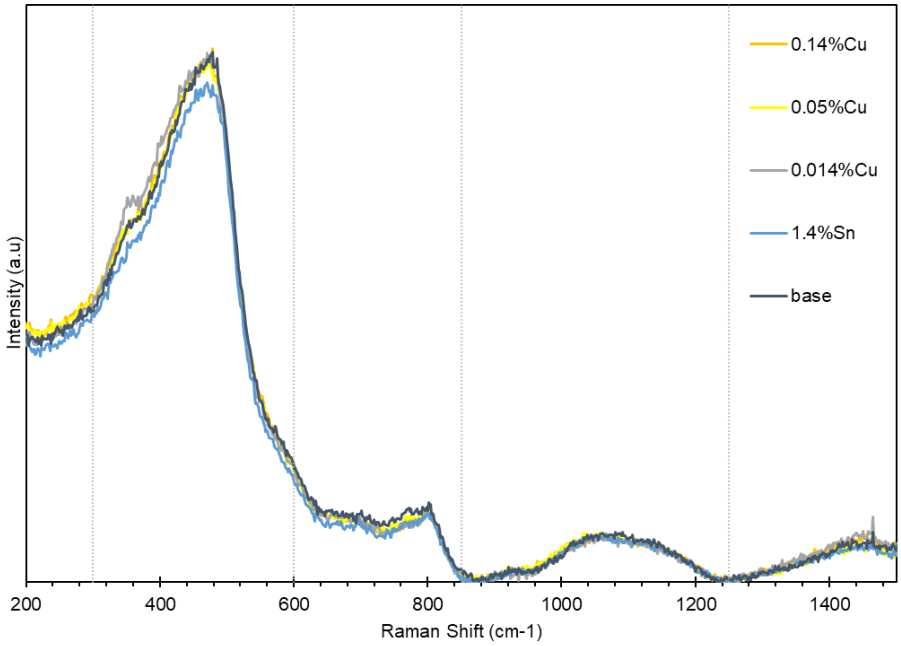

Figure 4.6 - Raman Spectra for Base Glass (base), 1.4% Sn, 0.014% Cu, 0.05% Cu and 0.14% Cu.

Raman modes from 400 to 850 cm^{-1} were already associated with the two ordered superstructures reedmergnerite $[BSi_3O_8]^-$ and danburite $[B_2Si_2O_8]^{2-}$ [39],as well as tri-,tetra- or penta-borate structures that arise from splitting of boroxol rings (B_3O_6) whose vibrational mode is found at 800 cm^{-1} [40].

Deconvolution of the Raman bands in the high frequency interval of 850-1250 cm^{-1}, associated with the asymmetric vibration of SiO_X structures[40], specifically related to Q_2^{Si} at 850 and 950 cm^{-1}, Q_3^{Si} at 1000, 1050 and 1080 cm^{-1}, and Q_4^{Si} at 1150 cm^{-1}, was also performed (table 4.2; figure 8.4). Three gaussian bands were obtained for each sample correspondent to the structural identification of $\boldsymbol{Q_2^{Si}, Q_3^{Si}, Q_4^{Si}}$ structural units, whose peaks show Raman shifts at approximately 920, 1050 and 1150 cm^{-1}. Analysis of the value of the area peak of each of the deconvoluted gaussian bands shows that tin and copper doping induce a variation which indicates formation of $\boldsymbol{Q_4^{Si}}$ structural units,

through increase of 8% of area value in detriment of Q_3^{Si} units. Although tin oxide doping shows the slight decrease in Q_2^{Si} structural units, this change is not observed with copper doping.

Table 4.2 - Raman shift of Q_2^{Si}, Q_3^{Si}, Q_4^{Si} structural units obtained in the deconvolution of Raman spectra in the 850-1250 cm^{-1} region for tin oxide doped samples.

		Q_2^{Si}	Q_3^{Si}	Q_4^{Si}
Base Glass	σ (cm^{-1})	19.3	57.7	38.5
	μ (cm^{-1})	921.8	1058.9	1155.3
	A%	4.0	72.6	23.4
1.4% Sn	σ (cm^{-1})	17.7	55.2	41.2
	μ (cm^{-1})	921.3	1049.0	1150.8
	A%	3.3	67.3	29.4
0.14% Cu	σ (cm^{-1})	19.4	55.2	43.4
	μ (cm^{-1})	920.1	1045.6	1149.2
	A%	3.9	64.3	31.7

4.2.4. Dilatometry

Thermal analysis was performed through dilatometry measurements (table 4.3). Thermal expansion coefficient analysis show a similar behaviour to what was previously found for tin oxide doped samples, values show great magnitude similarities, and a similar tendency, the value rises up to 7.4 x 10^{-6} for 0.05% Cu concentration, followed by a decrease trend correlated with copper doping. The working temperature is apparently stable throughout the doping procedure.

Table 4.3 - Dilatometry analysis results for tin oxide and copper doped samples. Glass Transition Temperature (Tg), Softening temperature (Ts), and Coefficient of Thermal Expansion (CET).

Sample	CTE $_{25\text{-}350ºC}$ x10^{-6} (K^{-1})	Tg (ºC)	Ts (ºC)
BG	6.91	493	533.3
1.4%Sn	6.85	492.4	-
0.014%Cu	7.35	488.3	526.5
0.03%Cu	7.05	489.2	549.3
0.05%Cu	7.40	493.8	536
0.08%Cu	6.94	493.2	529.7
0.14%Cu	6.64	496.5	526.4

Taking the base glass (BG) as reference, glass transition temperature results show how tin and copper oxide originate a slight value decrease, from 493 ºC to 488.3 ºC. Further copper doping induce an increasing tendency with the higher doped copper sample presenting a value of 496.5 ºC,

a value whose magnitude Is quite similar to the base glass analysis. Comparison between the base glass preparation at 1400 ºC and at 1550 ºC show a higher value for 1550 ºC which may be correlated to a higher degree of matrix organization.

Regarding the softening temperature values (Ts), results follow a similar trend, where the value is reduced for low copper concentrations and subsequently increased as seen for sample 0.03% Cu, further amounts of doping present a decreasing trend of the value. The results demonstrate that doping is not affecting the global hardness of the glass.

4.2.5.UV / Vis spectroscopy

The optical transmittance spectra obtained for copper doped samples with the base glass as reference is shown in figure 4.7. As previously analysed a bathochromic shift effect derives from doping, associated with the deep-UV light absorption from Sn^{2+} and and Cu^{+} in the near-UV.[45]. Optical cut-off values were calculated for all samples, calculation was performed as described in previous chapter, table 4.4.

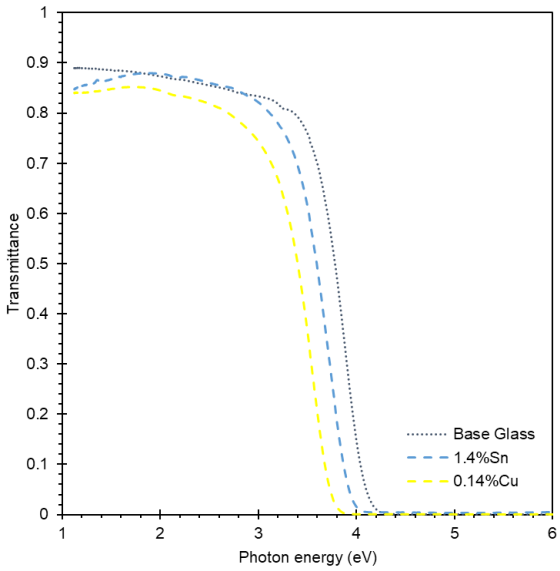

Figure 4.7 - Optical transmittance spectra of tin and copper doped samples melted at 1550 ºC with base glass as reference..

Results show a significant reduction of the cut-off edge from of the host glass and 1.4% Sn sample when compared to glasses melt at 1400ºC, the optimization procedure is apparently inducing a reduction of light scattering in the glass matrix.

Table 4.4 - Optical cut-off values for tin and copper oxide doped sample glasses, melted at 1550 ºC values in eV.

Sample	BG	1.4%Sn	0.014%Cu	0.03%Cu	0.05%Cu	0.08%Cu	0.14%Cu
Cutoff (eV)	4.25	3.92	3.95	3.89	3.85	3.84	3.77

4.2.6.Excitation spectra

Figure 4.8 shows the excitation spectra profile for all samples while monitoring light emission at 3.2 eV. Excitation spectra of the samples show a broad excitation profile, tin oxide doping show the already observed high and low energy bands of excitation at approximately 5 eV and 3.9 eV. The excitation spectra profile show that both high and low energy bands are influenced by copper doping, revealing that the high energy peak becomes more intense than the low energy peak. Spectra deconvolution of the high energy peak show in fact the presence of two superimposed gaussian bands with 0.1 eV difference, at 5 eV and 5.1 eV, associated with tin oxide and copper oxide, respectively. Copper doping not only affects the spectra by varying its intensity, but also by varying the low energy peak position, it originates a blueshift of the low energy peak to higher energies, a phenomena related to the formation of Cu^{+}.

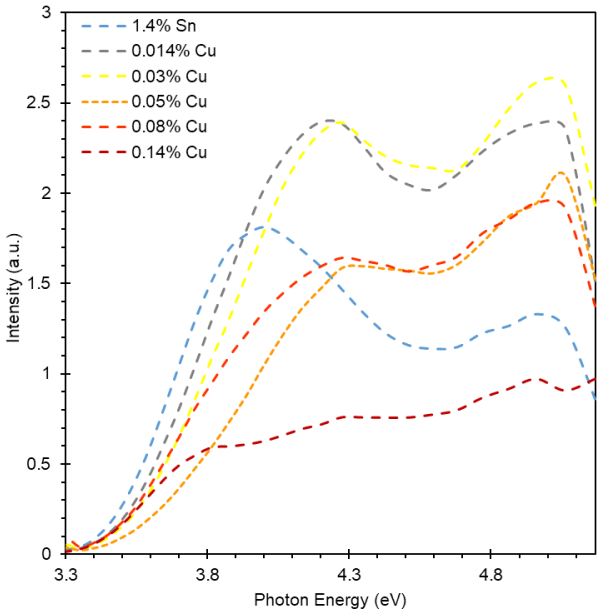

Figure 4.8 - PLE spectra of tin and copper doped samples, light emission monitored at 3.2 eV.

4.2.7.Emission spectra

Photoluminescence emission spectra (PL) of copper doped samples excited at 3.5 eV is seen in figure 4.9, with tin oxide doped glass shown as reference. It is observable how copper doping reduces the intensity of the high energy peak, and also how it influences the development of a broad lower energy peak at 2.1 eV, whose intensity increase is correlated with copper doping. An interesting feature of the system is the broad spectral range which surpasses the analysis technical limits, such behaviour is observed for both the emissive profile of tin oxide doped sample, but also to the copper doped system samples, with copper doping further extending these limits.

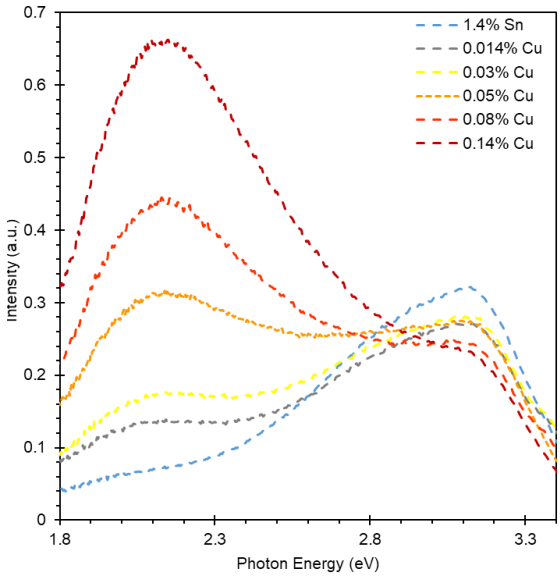

Figure 4.9 - PL spectra of tin and copper doped samples excited at 3.5 eV.

The nature of light emission of the system can be evaluated by varying the excitation energy and analysing the profile of light emission. Such has been performed for sample 0.08% Cu, whose results are found in figure 4.10. With excitation at 4.8 eV the emission band displays a maximum around 2.8 eV and a wing peaking at higher energies, showing that we have a predominant emissive contribution from Sn^{2+} and Cu^{+} ions. By lowering excitation energy a notorious trend is found, the emissive maximum is gradually redshifted. For lower energies, 3.4 eV, the emissive peak is located at 2.1 eV, while the high energy wing is gradually less intense. This indicates a gradual change of the emissive centres light emission, while higher energy excite both Sn^{2+} and Cu^{+}, lower energy enable the observation of a predominant Cu^{+} light emission.

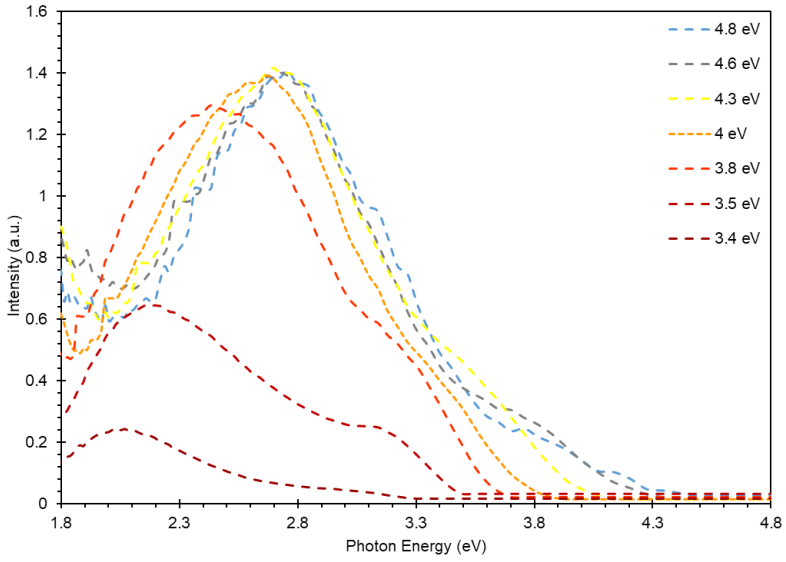

Figure 4.10 - Emissive profile dependence on excitation spectra for sample 0.08% Cu.

For high excitation energy the observed luminescence towards the blue contains a significant contribution from tin oxide owing to triplet to singlet ($T_1 \rightarrow S_0$) transitions, whereas emission to the red arises from $3d^9\ 4s^1 \rightarrow 3d^{10}$ transitions in Cu^+ ions, whose nature will be later evaluated.

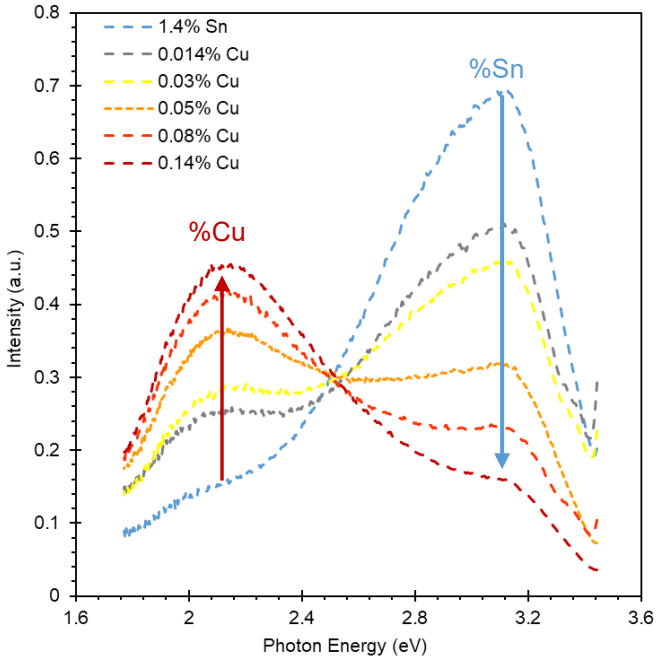

Figure 4.11 – Area normalized PL spectra of tin and copper doped samples excited at 3.5 eV.

Area normalization of the emissive spectra, figure 4.11, allows the analysis of the luminescent concentration quenching effect, doping induce a progressive inhibition of Sn^{2+} emission, while Cu^+ emission is seen to progressively increase its intensity. The spectra clearly identifies tin and copper oxide independent emission and the observation of an isoemissive point relating the total intensity of light emission.

4.2.8. Photoluminescence Kinetic Decay

Photoluminescent kinetic decays were performed for all samples through a global analysis fit achieved with a tri-exponential function, table 4.5. Results show consistent values over distinct doping amounts, where it is possible to distinguish three average values according to their order of magnitude. A short decay time is found with an average value of 7.7 μs representing the short decay triplet state of Sn^{2+}, and a second intermediate average decay time of 16 μs correspondent to the emission of tin oxide aggregates.

Table 4.5 - Photoluminescence kinetics decay time for tin and copper oxide doped samples (μs).

	1.4% Sn	0.014% Cu	0.03% Cu	0.05% Cu	0.08% Cu	0.14% Cu
τ_1	7.9	6.0	7.3	7.0	9.8	8.2
τ_2	16.2	15.7	14.9	15.8	17.7	15.7
τ_3	-	43.5	38.0	52.7	62.4	54.0

The longer decay time with an average value of 50 μs is correspondent to Cu^{+} forbidden triplet state emission, a value which is in good accordance with the slow decay time obtained by Debnath for copper emission in a glass matrix[46].

The pre-exponential factors obtained from the global fitting process, and their relation with the luminescence decay time can be evaluated for sample 0.14% Cu, figure 4.12. Here one can observe the energy dependence of each of the decay times obtained and their overall weight, clearly showing a structured emissive profile whose origin derives from three sources of light emission.

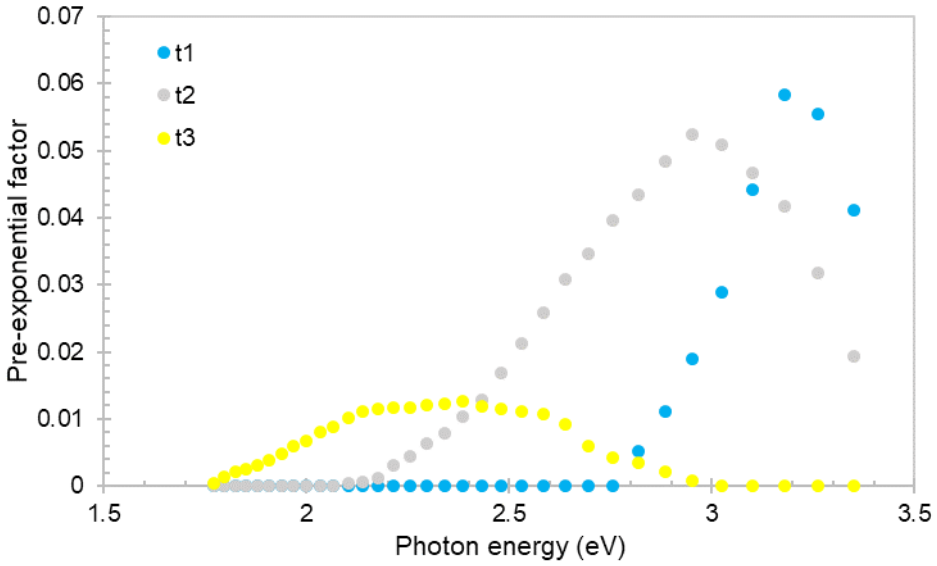

Figure 4.12 - 0.14% Copper sample global population decay analysis.

Sn^{2+} emission is responsible for the shorter decay times seen at higher energies, the faster luminescence light emission decay is found between 3.5 and 2.8 eV. Two-fold coordinated tin oxide centres show a slower luminescence profile, and its emission is responsible for a broad tail between 3.5 eV and 2 eV, reflecting the heterogeneous coordination of these structures. The longer time decay constants origin is Cu^{+} ions, for which a large tail arises in spectral domains of lower energies, from 3 eV to 1.7 eV.

4.2.9. Quantum Yield

Luminescent quantum efficiency measurements were obtained through the absolute method and measured at different excitation energies, 4.1 eV, 3.8 eV and 3.4 eV. Results, figure 4.13, show the increase of quantum efficiencies to 58% for concentrations larger than 0.03% Cu. When excited at 4.1 eV, SnO and CuO are the main light absorbers, while at lower energies the glass matrix responsibility over light absorption is increased.

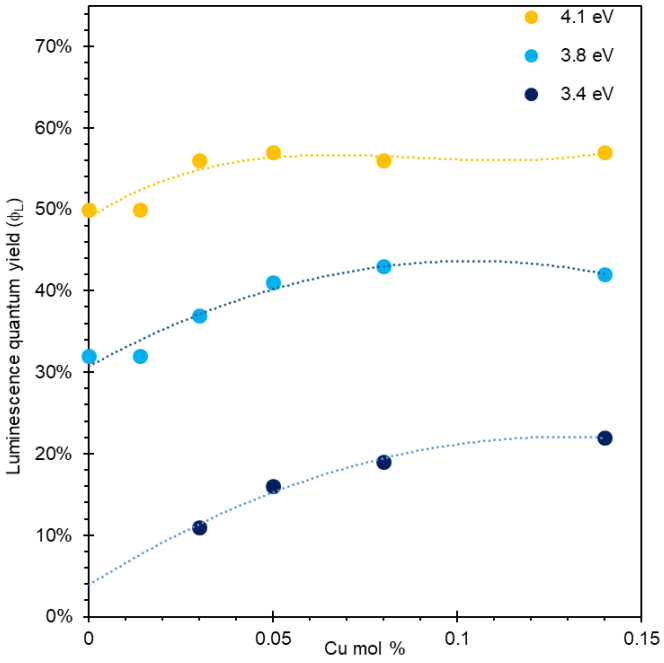

Figure 4.13 - Quantum yields for copper doped samples, with excitation energy at 4.1 eV, 3.8 eV and 3.4 eV.

4.3. *Conclusions*

The obtained tin and copper oxide doped glasses show a colour gradient from blue to white and yellow colour, figure 4.14, whose colour variation depends on the amount of copper doping inserted into the sample. The amorphous profile of the samples is seen through X-ray diffraction analysis which also introduce the observation of quartz formation. A feature which is also revealed through solid state NMR analysis, the study of ^{29}Si ^{11}B and ^{23}Na.which did not reveal any structural induced changes from tin or copper oxide doping.

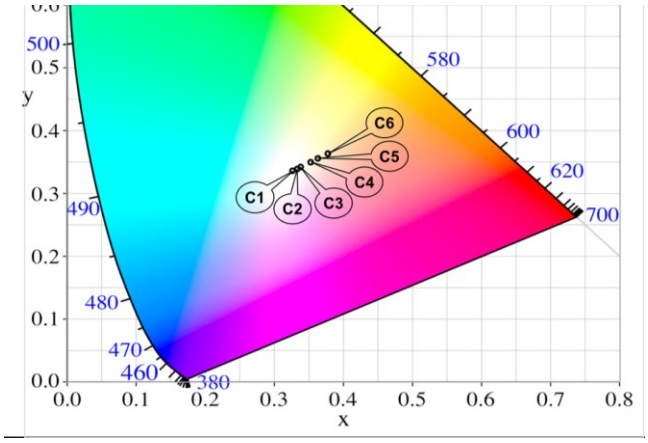

Figure 4.14 - Colour coordinates of tin and copper doped samples, excitation at 4 eV.

Raman spectroscopy reveals a similar profile to what was previously obtained with tin oxide doped samples. Development of interaction between both primary structural networks is revealed through the formation of the ordered macrostructures reedmergnerite $[BSi_3O_8]^-$ and danburite $[B_2Si_2O_8]^{2-}$, and the formation of boroxol rings (B_3O_6). Minor interactions are observed over the

silicate network, where copper doping induce the formation of 8% more $\boldsymbol{Q_4^{Si}}$ structural units over $\boldsymbol{Q_3^{Si}}$ structural units, and a residual negative variation of 0.1% for $\boldsymbol{Q_2^{Si}}$ structural units.

Thermomechanical properties of tin and copper oxide doped samples analysis reveal that neither glass transition temperature nor melting temperature show a high degree of variance, the thermal expansion coefficients results are also stable and of a similar magnitude.

Light absorption show a UV cut-off edge of 4.25 eV for the host glass, a value which is shown to increase with doping by 0.48 eV, for the larger amount of copper. These values suggest that the temperature increase procedure was effective in reducing absorption heterogeneities in the samples, as the host glass UV cut-off edge is shifted to higher energy values. Tin oxide doping reveals that inhomogeneous emissive centres are still developed, which is confirmed through time resolved photoluminescence. A broad emissive profile due to the formation of tin oxide aggregates is shown to extend due to the insertion of copper oxide, from 5 eV to 1.4 eV.

Copper doping excitation peak is superimposed with the high energy excitation peak of Sn^{2+} located in the deep-uv region at 5.1 eV and 5 eV, respectively. A third excitation channel correspondent to the low energy tin oxide excitation band is found at lower energies, 4.3 eV, a peak which is progressively inhibited with copper doping.

The nature of the systems light emission is characterized through a tri-exponential decay profile, correspondent to forbidden triplet to singlet electronic transitions. Three structural luminescent centres are unveiled, tin oxide (Sn^{2+}), tin oxide aggregates and Copper oxide (Cu^{+}), with kinetic decay values of approximately 8.2 μs, 15.7 μs and 50 μs, respectively.

Reorganization energy of the emissive and ground state was evaluated for sample 0.14% Cu. Excitation at 5 eV develops a maximum light emission at approximately 2.8 eV. This represent a large Stokes shift of 2.2 eV a value which clearly shows the potential of these samples to LSC development, with negligible photon reabsorption for Cu^{+}. Quantum efficiencies reached a peak value of 57% for copper concentrations of 0.03% and higher, with no luminescence quenching being detected

Taking into account the observed results, the photoluminescent pathways may be schematically represented as in figure 4.15.

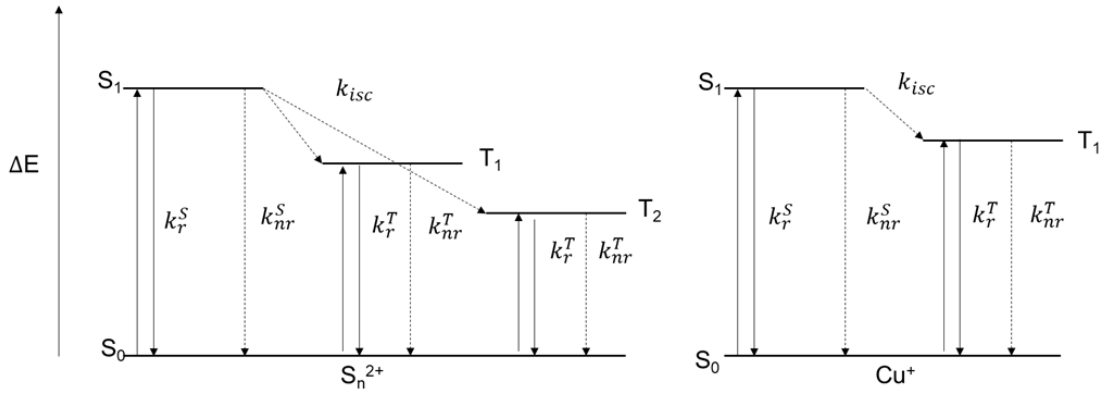

Figure 4.15 - Proposed scheme of electronic levels and related radiative (full-line) and non-radiative (dashed line) processes accounted for the analysis of PL emission of Sn and CuO doped samples.

5. Thin Film sputtering

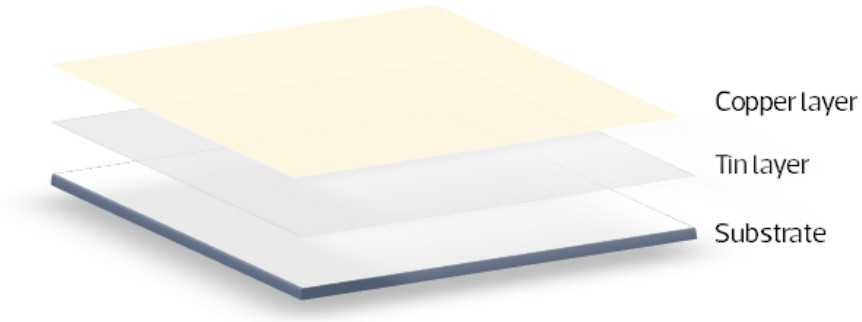

Figure 5.1 - Thin film metallic layer sputtering deposition example scheme.

Primary studies on thin film sputtering will be attempted in order to achieve photoluminescence. Copper and tin were sputtered through variation of the oxygen flow which will allow the identification of optimum conditions that induce the formation of Cu_2O and SnO, these will be later used for an alternate layer deposition. To evaluate if these elements diffuse through the substrate glass matrix, thermal treatment of the obtained samples was also performed. Development of thin films was monitored through Perfilometry, Raman spectroscopy and X-ray diffraction.

5.1. *Deposition procedure*

Plasma was always ignited in an atmosphere composed of 60% argon and variable oxygen flow, with chamber base pressure set to 10^{-3} mbar. Distinct gas channels were directed towards the chamber with gas flow being measured by mass flow controllers. Two different magnetron shutters were used to hold metallic copper and tin targets in order to avoid cross-contamination between the sources, since the target surface can adsorve contaminants from the air each time the chamber is open to change the substrate The substrate was top-mounted and the substrate sizes were uniform, 100x100x1 mm.

Each deposition process was run at room temperature, with a 5 minute pre-sputtering conditioning step performed with a closed shutter, to avoid contamination, allowing the target to stabilize with the deposition conditions being used. Oxygen flow will be expressed relative to the total gas flow, in units of standard cubic centimetres per minute (sccm). With the purpose to evaluate if diffusion is achieved toward the glass matrix the behaviour of copper and tin films under thermal treatment will be analysed.

5.2. *Copper/Tin sputtering with variable oxygen flow*

With a total of six samples being prepared, table 5.1, deposition time was of 30 min with 60% Argon flow and oxygen flow between 10% - 15% sccm, and 45 min for oxygen flow between 20% - 30% sccm. Deposition height was evaluated by perfilometry. Thermal treatment will be performed for one hour, in air, at constant temperature, in 100 ºC steps.

Table 5.1 – Copper (CFx) and tin (TFx) thin film samples, deposition time and height.

Sample	Cu x%O_2 (sccm)	deposition time (min)	deposition height (nm)
CF1	10%	30 min	207.9
CF2	12.5%	30 min	195.5
CF3	15%	30 min	238.5
CF4	20%	45 min	343.3
CF5	25%	45 min	361.5
CF6	30%	45 min	314.8

sample	Sn x%O2 (sccm)	deposition time (min)	Height (nm)
TF1	0%	30 min	78.6
TF2	2%	30 min	73.8
TF3	4%	30 min	76.3
TF4	6%	30 min	80.9
TF5	8%	30 min	76.0

5.2.1.Results

5.2.2. Oxygen flow variation for copper and tin thin films

XRD analysis (figure 5.2) of sample deposition show for all samples the amorphous profile of the substrate through a large band at 22º 2θ, and the evolution of copper oxide formation dependent on oxygen flow. Tin oxide sample 4% O_2 is shown since no crystalline diffraction pattern was observed for the whole batch of tin sputtered samples. Regarding the development of copper oxides, XRD analysis reveal crystalline patterns for the development of metallic copper [47]at 43.3º 2θ for higher values of oxygen flow, 20% O_2 and 25% O_2, and low values of 5% O_2. Intermediate flow of oxygen, 12.5%, reveal the absence of metallic copper diffraction pattern, instead a distinct diffracting peak at 42.3º 2θ, associated with the crystalline structure of Cu_2O, and a second diffracting peak at

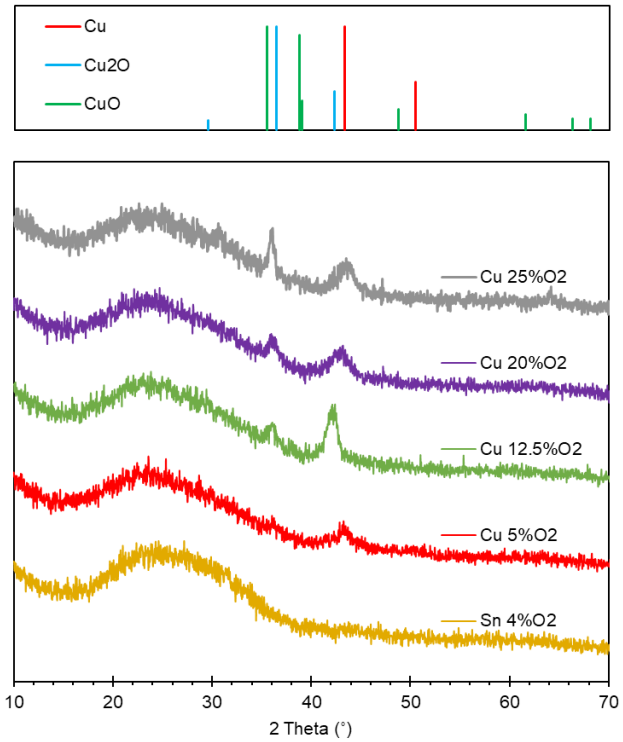

Figure 5.2 - XRD spectra of copper and tin samples with variable oxygen flow.

33º 2θ associated with the peak overlap of Cu_2O and CuO, being found for oxygen flow greater than or 12.5% O_2. [48]

Figure 5.3 shows the Raman spectra of copper (a) and tin oxide (b) thin films with deposition performed at different partial oxygen pressures. Both spectra show at 1100 cm^{-1} a broad peak formation which is unrelated to copper or tin oxide formation due to its large Raman shift, this peak was previously associated with the asymmetric vibration of SiOx structures [40], we are observing the substrate glass. Figure 5.3 (a) shows the influence of oxygen over development of a copper oxide crystalline phase, characterized through the formation of two well defined peaks at 530 and 625 cm^{-1} as for example in sample Cu 20% O_2. These peaks are present in the majority of samples, exception made for Cu 30%O_2. Analogous peaks are found with the Raman spectra of crystalline and amorphous-crystalline Cu_2O[49], where the 530 cm^{-1} peak is an allowed Raman mode according to the selection rules, and the 625 cm^{-1} peak represents a forbidden transition, it arises from frequency resonance with other excitons due to imperfections of the crystalline structure of copper oxide [50].

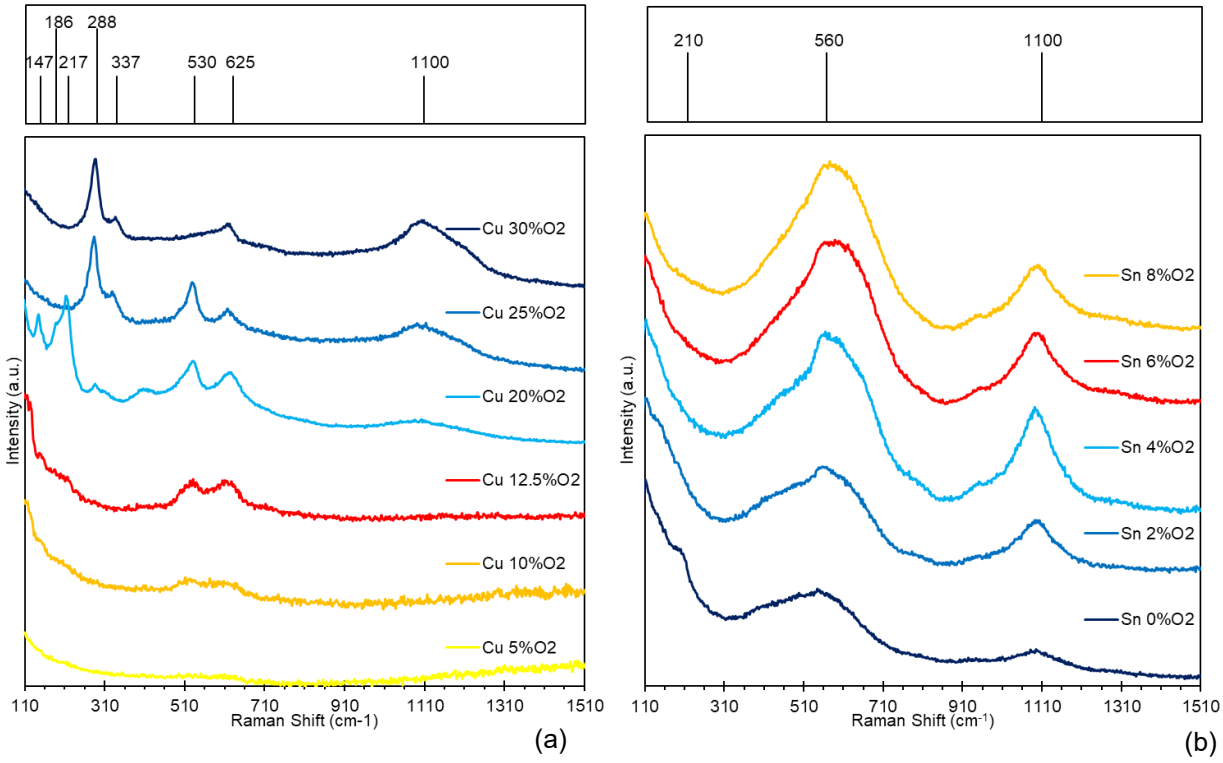

Figure 5.3 - Raman spectra of copper thin films (a), and tin thin films (b), obtained with variable oxygen fluxes.

Sample Cu 20% O_2 spectra show several features to analyse, a copper related Raman shift can be found at 147 cm^{-1} where a forbidden mode is observed, it results from the selection-rule violation due to the imperfect crystalline structure of Cu_2O. Raman modes at 186 and 217 cm^{-1} are also associated with Cu_2O , representing second order overtones. At 288 cm^{-1} and 337 cm^{-1} two residual peaks are found to gain intensity with higher percentage of oxygen flux, these are analogous Raman modes for CuO identified elsewhere [51]. The two Raman modes at 530 and 625 cm^{-1} had already been identified as Cu_2O active modes.

While it is noticeable that Cu_2O is formed with increasing oxygen flow, until 12.5% O_2, further oxygen flux induce the coexistence of two crystalline phases of both Cu_2O and CuO, as seen for sample Cu 20% O_2. The inhibition of Cu_2O allowed transitions for higher oxygen fluxes show that the crystalline structure of CuO plays a major role of formation under greater oxygen flow conditions.

Tin thin films show similar Raman features for all samples, figure 5.3 (b), with two broad peaks at 560 and 1100 cm^{-1} dominating spectra appearance. While the peak as 1100 cm^{-1} was already accessed, the broad peak at 560 cm^{-1} is representative of spectral overlap of three Raman bands at 472, 630 and 560 cm^{-1} [52].The first two peaks are analogous to single-crystal or polycrystalline SnO_2, and results show that their intensity is reduced with oxygen flow, while the third peak, associated to the formation of nanometric SnO_2 powder, is further intensified with increasing oxygen flow. These results reflect the stability of SnO_2 crystalline structure, which is being formed independently of oxygen flow, which, when subject to higher oxygen flow tend to deteriorate into small grain sized SnO_2.

5.2.3. Thermal treatment of Copper Oxide thin films

Temperature influence on the development of the crystalline structures of sample Cu 10% O_2 was evaluated with Raman spectroscopy, figure 5.4 (a) and X-Ray diffraction, figure 5.4 (b). The Raman modes at 125 cm^{-1}, 147 cm^{-1} and 625 cm^{-1} are forbidden from the selection rules, its development with temperature indicate deformation of Cu_2O crystalline structure. Such assessment is corroborated from the development of the second order overtone mode at 216 cm^{-1} and the fourth order overtone at 420 cm^{-1}, which are intensified with temperature. The allowed mode at 530 cm^{-1} is persistent and sharper with temperature increase, indicating the stability of crystalline Cu_2O phase.

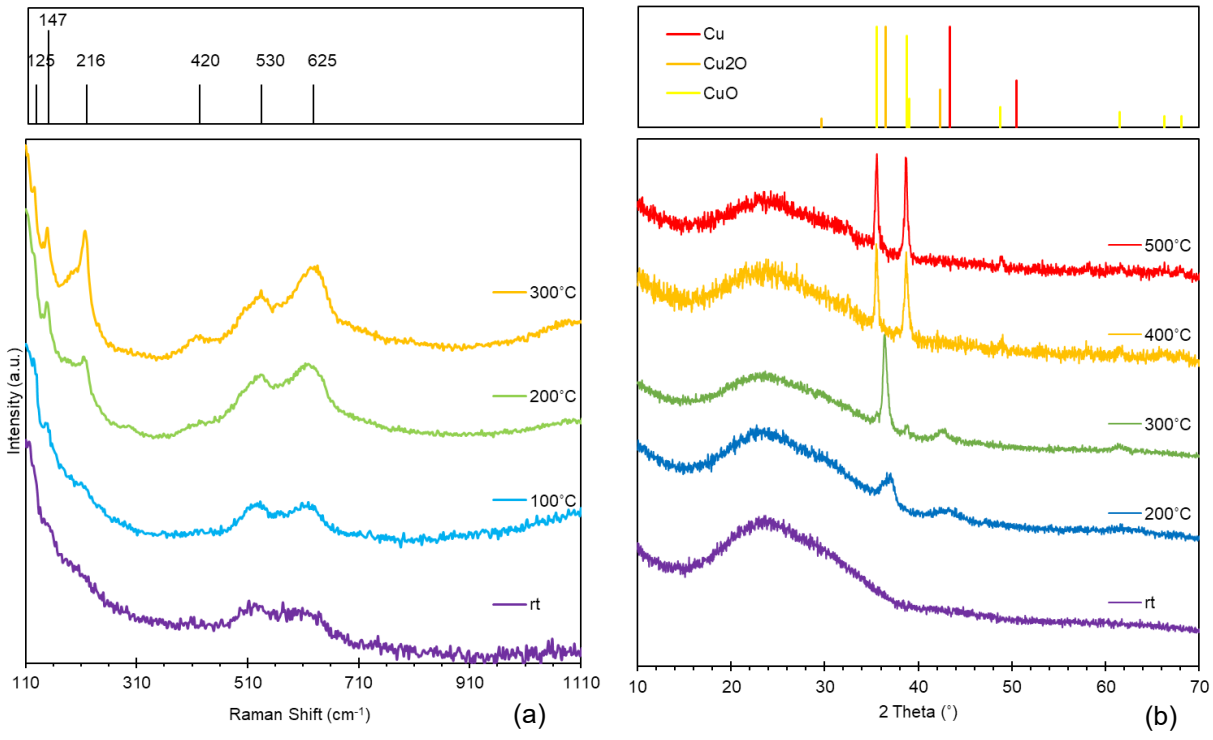

Figure 5.4 – (a) Raman spectra of Cu 10% O_2 sample, annealed at distinct temperatures and (b) XRD Maximum Normalized Copper 10% O_2 sample, annealed at distinct temperatures, (rt) room temperature.

Such observations are corroborated from XRD analysis where Cu_2O diffraction peak is found to steadily develop from until 300 ºC temperature is reached, after this temperature only CuO crystalline diffraction peaks are displayed.

5.3. *Sn / Cu sandwich thin film*

Having in mind the possibility to develop luminescence at the interface of both tin and copper oxides, a multilayer thin film was development. Identification of an optimum value of oxygen flow for copper deposition (12.5% O_2), and the realization of its thermal stability defined the copper sputtering procedure. Since Sn^{2+} crystalline structure has shown to firmly develop for intermediate values of oxygen flux, the argument used to decide an optimum oxygen flow was based on the greater transparency the \$%O_2 sample presented.

With the purpose of stabilizing copper oxide, tin oxide layers were deposited beneath and on top of each copper layer; two copper layers were deposited in total, thus creating a total of five alternate layer with deposition time of 10 min each. Deposition height was evaluated by perfilometry. Thermal treatment will be performed for one hour, in air, at constant temperature, in 100 ºC steps.

Table 5.2 – Copper and tin (CTF) multilayer thin film samples, deposition time, layer order and height (nm).

Sample	Cu x%O_2 (sccm)	Sn x%O_2 (sccm)	deposition (min)	Layer order	deposition height (nm)
CTF1	12.5%	4%	10 min per layer	SnxCuxSnxCuxSn	374.94

5.3.1. Results

XRD analysis, figure 5.5 (a) of the multilayer thin film show the amorphous profile of the substrate, characterized by a large band at 22º 2θ, and the evolution pattern of diffraction obtained. At room temperature a characteristic peak is identified at 36.4 2θ, and a small lump at 42.3º 2θ relative to the development of Cu_2O crystalline phase. The development of these peaks when subject to temperature is observable until 300ºC where the lower angle peak appears between two new features, at 35.5º and 38.7º 2θ, both correspondent to the crystalline phase of CuO [48]. Metallic copper is found to form at 400ºC through the appearance of a crystalline peak at 43.3º 2θ [53]. A relevant result at this temperature is the identification of peaks related to the development of Cu_2O crystalline phase, identified at 36.4 2θ and 42.3º 2θ. At 500 ºC Cu_2O isn't detected, two features are however observed which indicate further oxidation of copper, at 38.7º 2θ and 35.5º 2θ the diffracting peaks are analogous to crystalline CuO[48].

Raman spectroscopy, figure 5.5 (b) show two Raman modes at 530 cm^{-1} and 625 cm^{-1} already identified as analogous to Cu_2O crystalline phase active modes. The results corroborate the formation of Cu_2O for temperatures until 300 ºC, where, although the amount of noise in the spectra, the allowed Raman peak at 625 cm^{-1} is identified, while the forbidden transition peak at 530 cm^{-1} has disappeared.

Associated with the formation of CuO, the vibrational Raman mode at 276 cm^{-1} is also identified[51].Temperature dictates the stability of the crystalline structure, with its increase, other

spectral features arise, associated with Cu_2O, such as the 147 cm^{-1} forbidden mode and the second order overtone at 216 cm^{-1}.

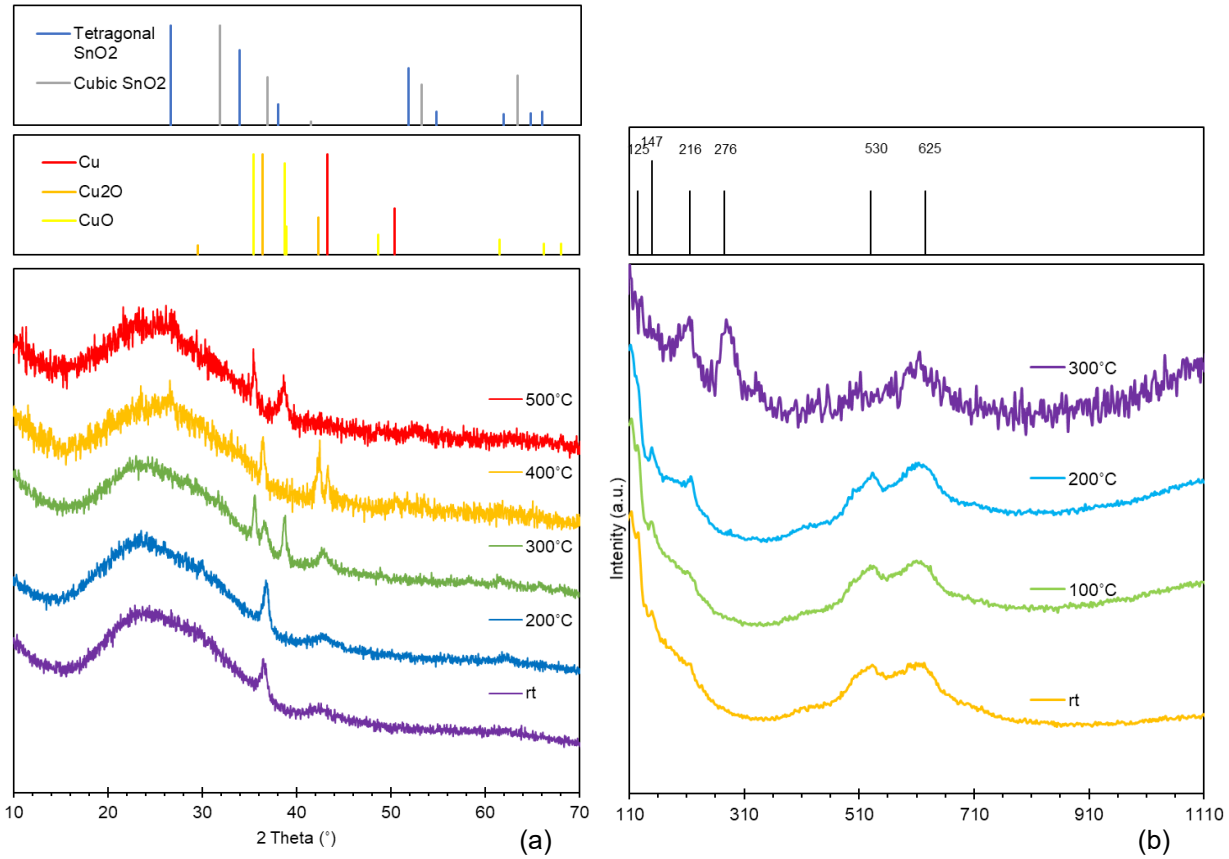

Figure 5.5 - (a) XRD Maximum Normalized Cu/Sn multilayer, annealed at distinct temperatures, (rt) room temperature. (b) Raman spectra 5x Copper 12.5% O_2 and Sn 4%O_2 sandwich samples annealed at distinct temperatures.

5.4. *Conclusions*

Development of thin film sputtering show the development of Cu^+ crystalline structure for optimum oxygen flow of 12.5%, while Sn^{2+} crystalline structure has shown to firmly develop for intermediate flux values, 4%O_2 with samples showing a high transparency degree. Having achieved the development of a Cu^+ thin film protected with a SnO layer, we have increased the stability of copper oxide to temperature, the 300 ºC barrier that arose as a generic value for stability of a crystalline Cu_2O was surpassed by at least 100 ºC, with Cu_2O being identified at 400 ºC.

Attempted diffusion of the crystalline structures onto the glass matrix did not reveal photoluminescence in the visible region, although it has been reported that Cu_2O crystals exhibit photoluminescent in the near infrared region. Although Cu^+ and Sn^{2+} have been formed, the phenomena may require requires quantum confinement conditions which were not obtained in sample preparation. We have observed a multitude of forbidden Raman modes and overtones which reveal that the development of thin films with heterogeneous layer overlap disturbs the oxide

structural arrangement. Optimization of the crystalline structure of the oxide might originate the quantum confinement conditions required for photoluminescence to take place.

6. Future views

We were able to develop luminescent glass prototypes extremely capable of UV-light down conversion. Tuning the concentration of the doping elements revealed three distinct colour tones to the visible red region characterized by high quantum efficiencies and large Stokes shift. These samples can be immediately tested for large area production and assembly in traditional photovoltaic cells or directed to new building blocks with integrated architecture for future net-zero consumption buildings. Moreover, the applicability of these materials is not restricted to solar harvesting, they may be applied as lasers, displays, LED lightening or other simple common end user applications as a warm light.

The perspectives on a future work for the development of photoluminescent thin films could be settled on the development of studies regarding the oxides ability to diffuse into the substrate matrix and posterior evaluation of the films properties. Also, the development of specific sputtering targets where the prepared copper and tin doped glass is assembled might develop the above mentioned confinement conditions which enable the photoluminescent phenomena. If this preparation is successful the development of photoluminescent thin films can suffer a major breakthrough with a fast, reliable and effective means to achieve a large area photoluminescent solar converter.

7. Bibliography

(1) René T. Wegh *et al*, Science 283, **1999,** 663**.**
(2) Report Report of the Ad hoc Working Group on defining critical raw materials, European Commission, **2014.**
(3) De-Chao, Y. *et al* Light: Science & Applications, **2015,** 4**.**
(4) Kumar, D. *et al* Journal of Nanoscience and Nanotechnology,17, **2017,** 3135–3145.
(5) Meinardi, F., *et al* Nature Photonics, **2017**
(6) Akkerman, Q.A., *et al* J. Am. Chem. Soc., 138, **2016,** 1010-1016**.**
(7) Jiménez, J. A., Optical Materials, 37, **2014,** 347–351.
(8) A. Yasumori, F. *et al* J. Electrochem. Soc. 159, **2012,** J143.
(9) Kuznetsov, A.S., *et al*, Nanoscale 5, **2013,** 10065
(10) H. Masai, et al. J. Mater. Chem. C 2, **2014,** 2137.
(11) E. Borsella, et al. J. Appl. Phys. 91, **2002,** 90.
(12) Cannizzo,a., Journal of Non-Crystalline Solids 352, **2006,** 2082–2089.
(13) Skuja, L. Journal of Non-Crystalline Solids, 149, **1992,** 77-95,
(14) Jiménez, Optical Materials 37 (2014) 347–351, Materials Chemistry and Physics 147/3, **2014**, 469-475.
(15) Yasumori, A. et al. Journal of The Electrochemical Society, 159 (5) J143-J147 (**2012**)
(16) Ruivo, A.; Andrade, S.M.; Rocha, J.; Laia, C.A.T.; Pina, F.; J. Phys. Chem. C, 118, **2014,** 12436−12442
(17) Ha, M.T. J. Am. Ceram. Soc., **2016,** 1–9.
(18) H.A. Atwater, A. Polman, Nat. Mater, 9, **2010,** 205.
(19) Zhang Ping et al, J. Semicond., 35, **2014 ,** 103001
(20) Journal of Alloys and Compounds 583, **2014,** 186–190,
(21) Meillaud, F. *et al*, Materials Today, 18, **2015,** 7.
(22) *Introduction to Glass Science and Technology*, J. E. Shelby, Royal Society of Chemistry, **2005**
(23) Turnbull, D. Contemp. Phys, vol. 10, no. 5, **1969**, 473-488
(24) A. Paul Chemistry of Glasses Springer **1982**
(25) *Molecular Fluorescence, Principles and Applications*, B.Valeur, Wiley-VCH **2001**
(26) *The materials science of thin films*, Milton Ohring Academic Press, **1992**
(27) Yadav, A.K., et al, RSC Adv., 5, **2015**, 67583-67609
(28) Rukang,L.; Journal of Non-Crystalline Solids 111, **1989**, 199-204.
(29) P. Kaur, S. Kaur, G. Pal Singh, D.P. Singh, J. Alloys Comp. 588, **2014,** 394.
(30) Laura Martel, J. Phys. Chem. C, 115, **2011,** 18935–18945.
(31) Sigel, George,H.; Optical Absorption of Glasses, Treatise on Materials Science & Technology, 12, **1977**, 17.
(32) A. Dietzel, Z. Electrochem, 48, **1942,** 9–23
(33) Schreiber, H.D. *et al*, Journal of Non-Crystalline Solids 181, **1995,** 225-230.
(34) Zhang Ping *et al*, J. Semicond, 35, **2014,** 103001.
(35) *Advanced Inorganic Chemistry*, F.A.Cotton, G.Wilkinson, John Wiley & Sons **1988**.
(36) Debnath, R.; Kumar S., Journal of Non-Crystalline Solids 123, **1990,** 271-274.
(37) Annu. Rep. Prog. Chem., Sect. C: Phys. Chem., **2012**, 108, 177
(38) Sherriff, B. L., *et al*, Eur. J. Mineral. **1991**,3,751.
(39) M. Wang, J. Cheng, M. Li and F. He, Phys. B, **2011**, 406, 3865.
(40) B. G. Parkinson, et al, J.Non-Cryst. Solids, **2008**, 354.
(41) Chiodini, N. et al, Journal of Non-Crystalline Solids 261, **2000,** 1-8
(42) Jiménez, Optical Materials 37, **2014**, 347–351.
(43) Gualtieri, A. F., Journal of Applied Crystallography 33, **2000**, 267-278.

(44) Freude, D., Encyclopedia of Analytical Chemistry John Wiley & Sons, **2000**, 12188–12224.
(45) Borsella, E. *et al*, J. Appl. Phys. 91, **2002** 90.
(46) Debnath , R. et al, Chemical physics letters 155, **1989,** 1.
(47) Swanson, Tatge., Natl. Bur. Stand. (U.S.), Circ. 539, I, **1953**, 15.
(48) Brese, N.E.; J. Solid State Chem., 89, **1990**,184.
(49) J. C. W. Taylor and C. L. Weichman, Can. J. Phys. 49, **1971**, 601
(50) P. F. Williams and S. P. S. Porto, Phys. Rev. B 8, **1973**, 1782.
(51) A. Compaan, and J. R. Macdonald, Phys. Rev. B 12, **1975**, 20.
(52) J. Zuo, et al. J. Appl. Phys. 75, **1994**,1835.
(53) Swanson, Tatge., Natl. Bur. Stand. (U.S.), Circ. 539, I, **1953**, 15.
(54) Mateker, W.; et al, Chem. Mater., **2015**, 27 (2), pp 404–407
(55) Yu, C., et al, J. Appl. Phys. 110, **2011**, 063526.
(56) Qiu, D., et al, Mat. Chem. and Phy. 111, 2–3, **2008**, 455-462
(57) Hansen, M.R., J. Phys. Chem. A, 108, **2004**, 586-594
(58) *Fundamentals of Photochemistry,* K. K. Rohatgi-Mukherjee, New Age International, **1978**.

8. Appendix

8.1. *Raman spectra deconvolution for tin oxide doped samples*

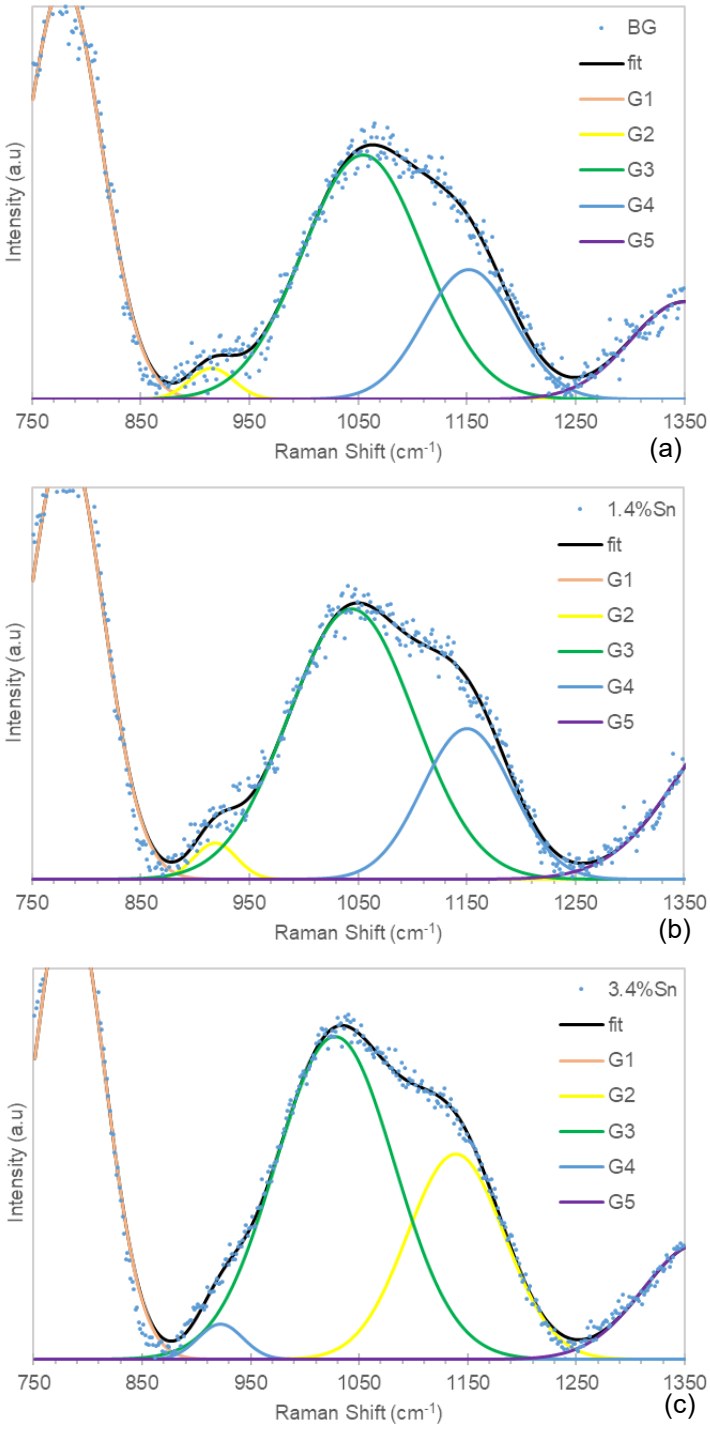

Figure 8.1 - Deconvolution of Raman spectra in the 850-1250 cm^{-1} region for tin doped samples (a) Base glass (b) 1.4% Sn (c) 3.4%Sn.

8.2. *Dilatometry results*

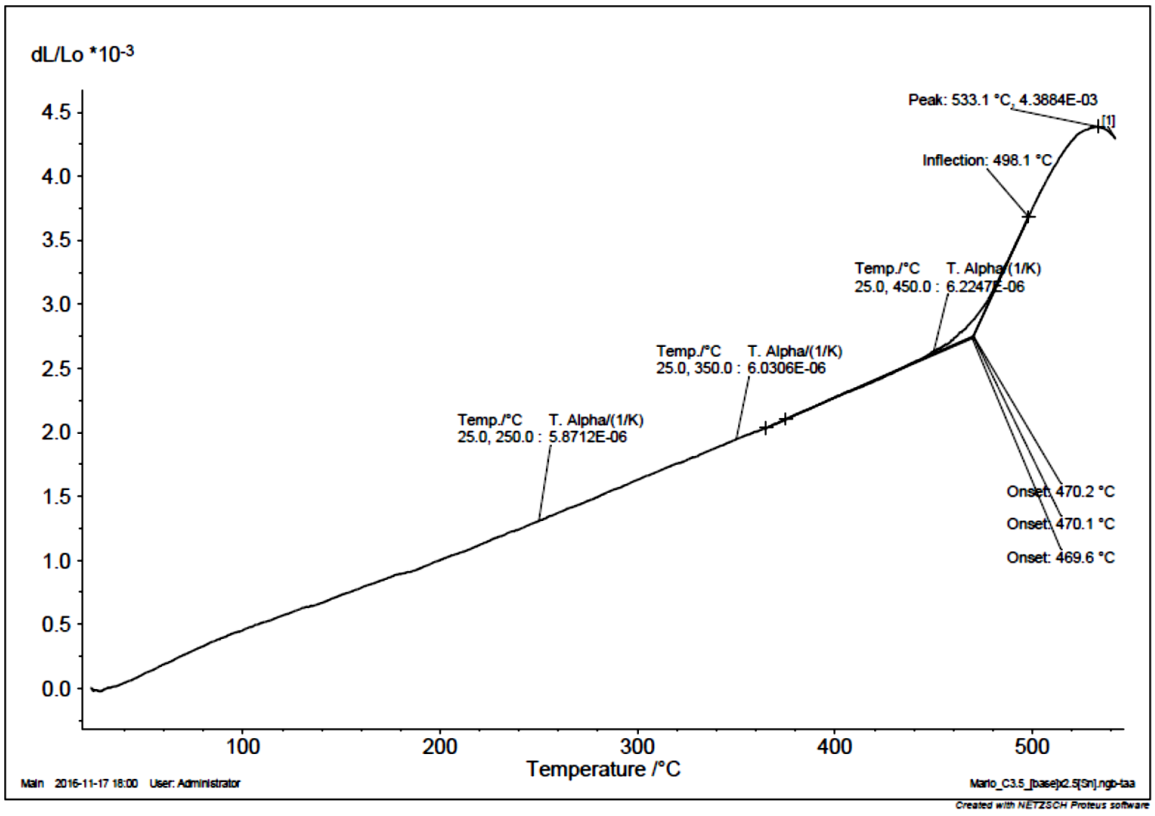

Figure 8.2 - Dilatometry analysis for sample 3.4% Sn.

8.3. *PLE/PL spectra of tin oxide doped glass samples*

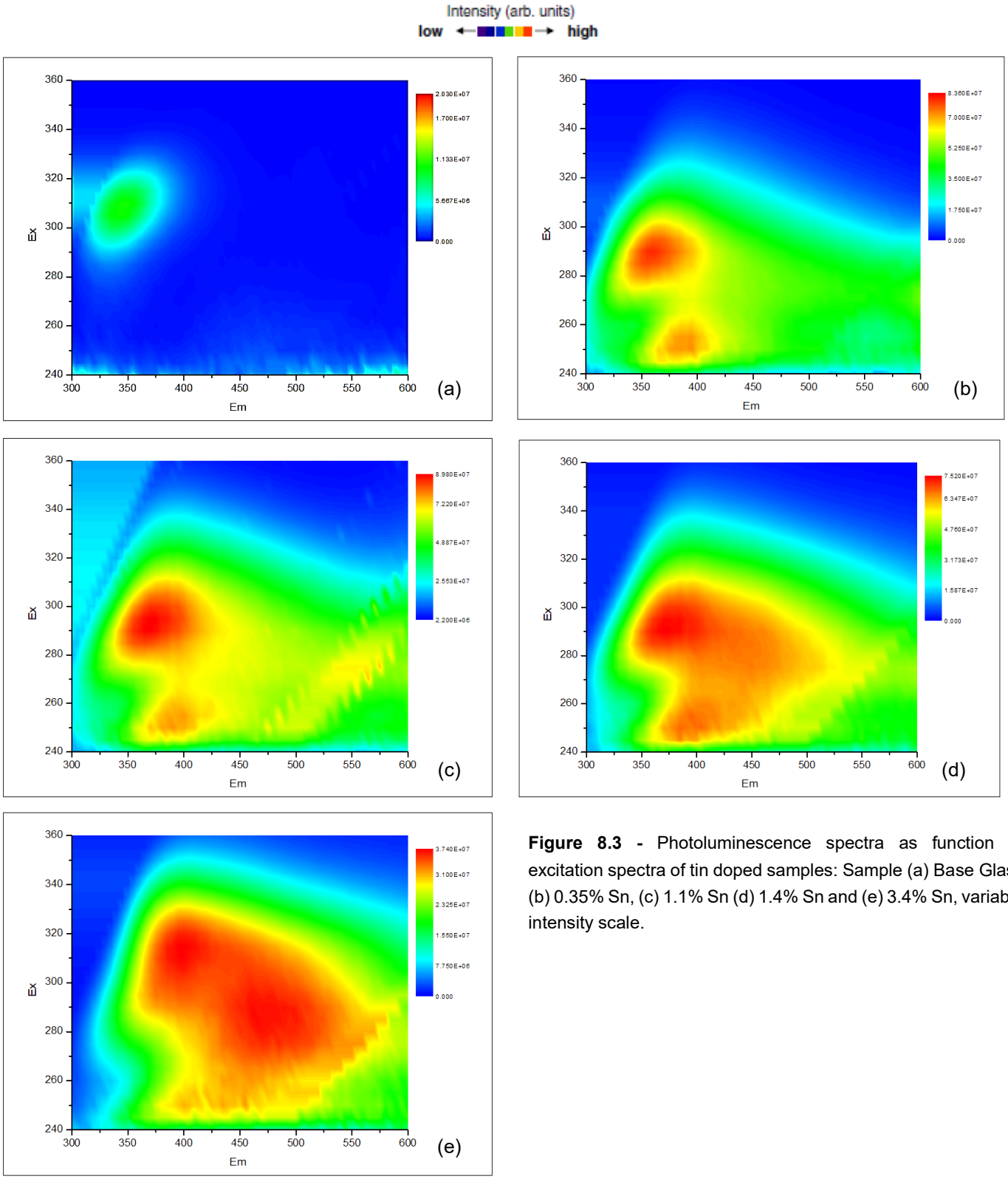

Figure 8.3 - Photoluminescence spectra as function of excitation spectra of tin doped samples: Sample (a) Base Glass (b) 0.35% Sn, (c) 1.1% Sn (d) 1.4% Sn and (e) 3.4% Sn, variable intensity scale.

8.4. *Raman spectra deconvolution for tin and copper oxide doped samples*

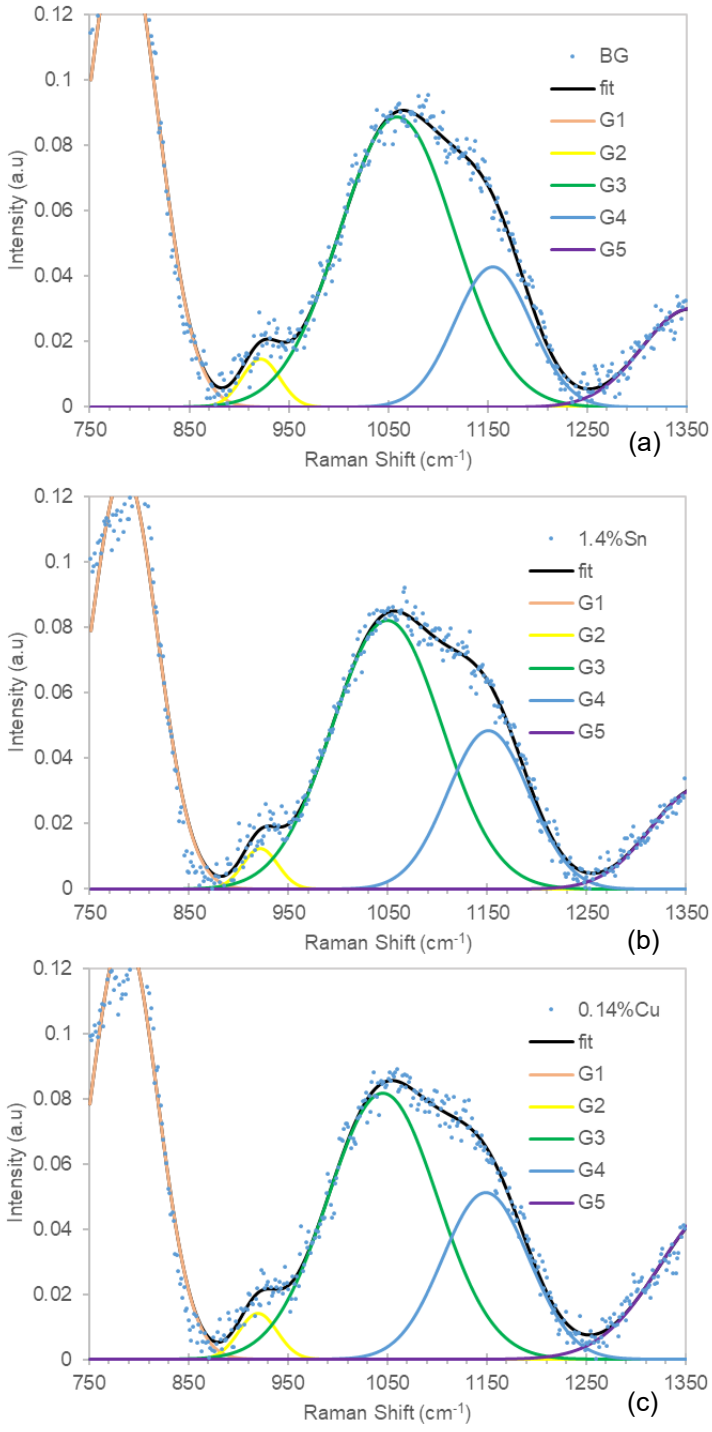

Figure 8.4 - Deconvolution of Raman spectra in the 850-1250 cm^{-1} region for tin and copper doped samples (a) Base glass (b) 1.4% Sn (c) 0.14% Cu.

8.5. *PLE/PL spectra of tin and copper oxide doped glass samples*

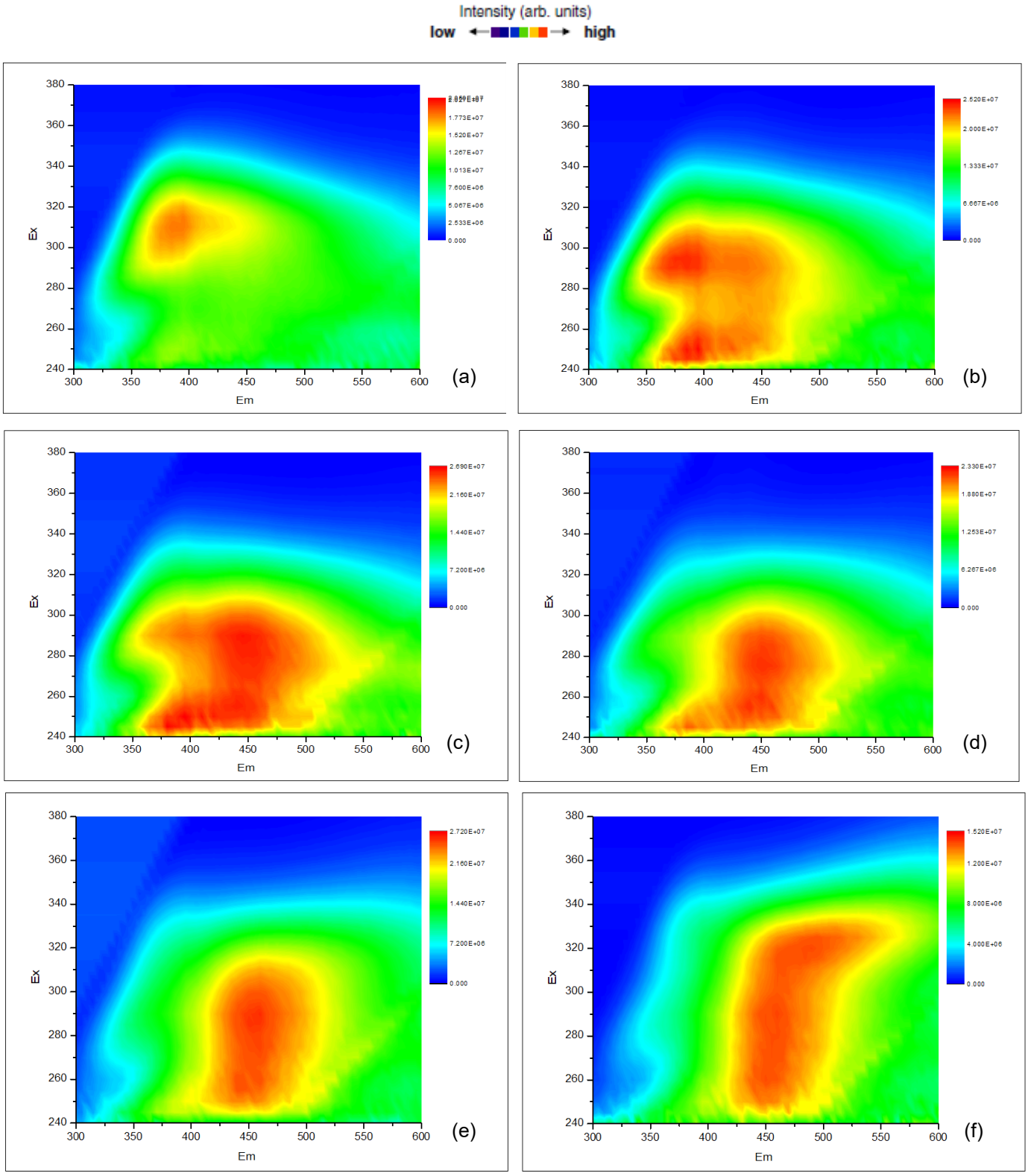

Figure 8.5 - Two dimensional Photoluminescence spectra as function of excitation spectra of tin and copper doped samples (a) 1.4%Sn, (b) 0.014%Cu, (c) 0.03%Cu, and (d) 0.05%Cu, (e) 0.08%Cu, (f) 0.14%Cu.

8.6. *Boron macrostructures*

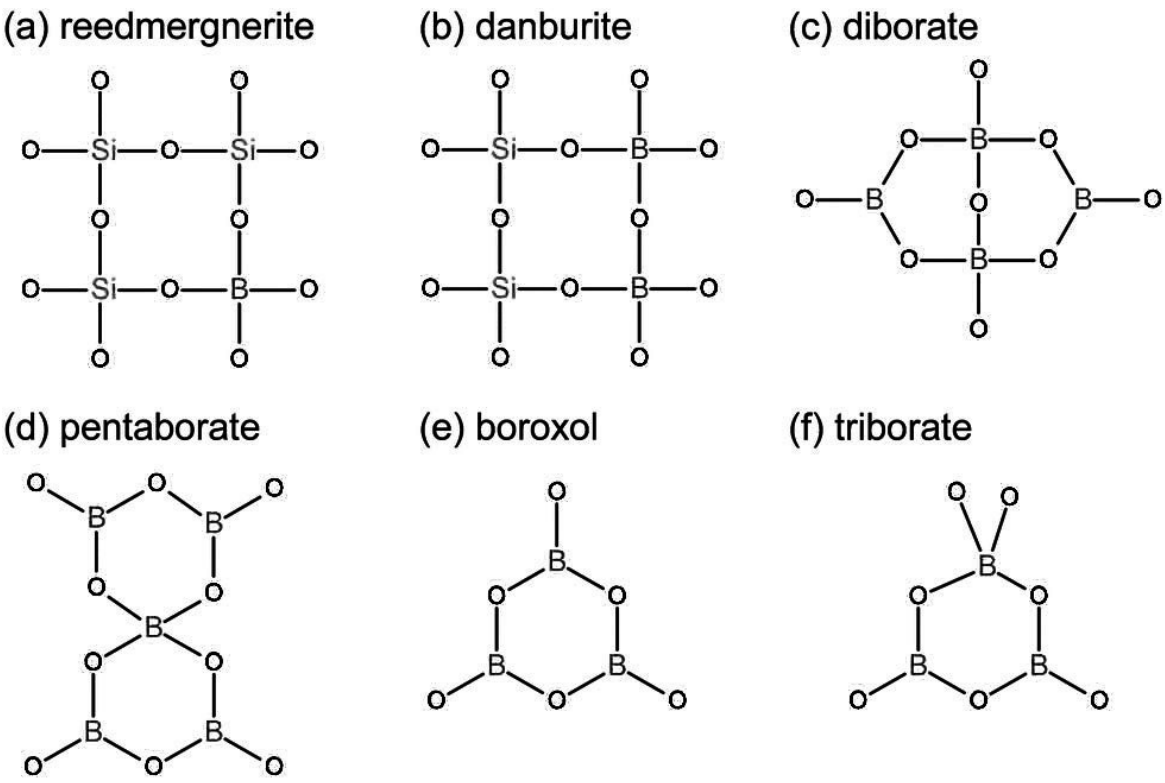

Figure 8.6 - Boroxol structures.

9. Supplementary information

Solid State NMR

^{29}Si NMR spectra were acquired on Bruker Avance III 400 spectrometer operating at B_0 fields of 9.4 T, with Larmor frequency of 79.5 MHz.

^{27}Al, ^{11}B and ^{23}Na NMR spectra were acquired on Bruker Avance III 700 spectrometer operating at B_0 fields of 16.4 T, with $^{27}Al/^{11}B/^{23}Na$ Larmor frequencies of 182,1/224,1/184,8 MHz. ^{27}Al magic angle spinning (MAS) experiments were performed on double-resonance 2,5 mm Bruker MAS probe

Raman spectroscopy

Glass doped samples: A Labram 300 Jobin Yvon spectrometer, equipped with a solid-state laser operating at 532 nm, was used.

Thin-Films: A Raman Microscope – Renishaw Qontor, equipped with 532 nm laser, was used.

X-ray diffraction

Glass doped samples: A Philips X'Pert MPD X-ray powder diffractometer using Cu Kα radiation, λ = 1.540598 Å, with step width 0.02°, was used.

Thin film samples: An X'Pert PRO MPD Multi-Purpose Diffractometer in a Theta-Theta configuration was used, with step width of 0.02°

Dilatometry

A Netvcshe Dil402PC dilatometer was used from 25 to 700 °C with a heating rate of 5 $K \cdot min^{-1}$. Samples were cut and polished with 2.5 cm wide and a diameter of 5 mm.

Dilatometry measurements analyse the change of volume of a material when it is subject to a temperature ramp, its results are usually obtained in the form of a thermal expansion spectra (figure 2.6), where enthalpy or volume are temperature dependent values.

Analysis of the results data allow the determination of three thermal constants of particular interest to investigate:

1. The thermal expansion coefficient (TEC) represents the temperature dependent expansion ability of a material, it is mathematically represented through the slope of the first linear portion of the thermal expansion data;

2. The glass transition temperature (T_g) represents the characteristic glass phase transition of a material, it is determined through the intersection of two straight lines extrapolated from the data;

3. The softening temperature (T_s) represents the temperature at which the viscosity of a glass reaches a limit value where it is still capable to prevent deformation of its own weight, it is determined from calculation of the maximum value of the data.

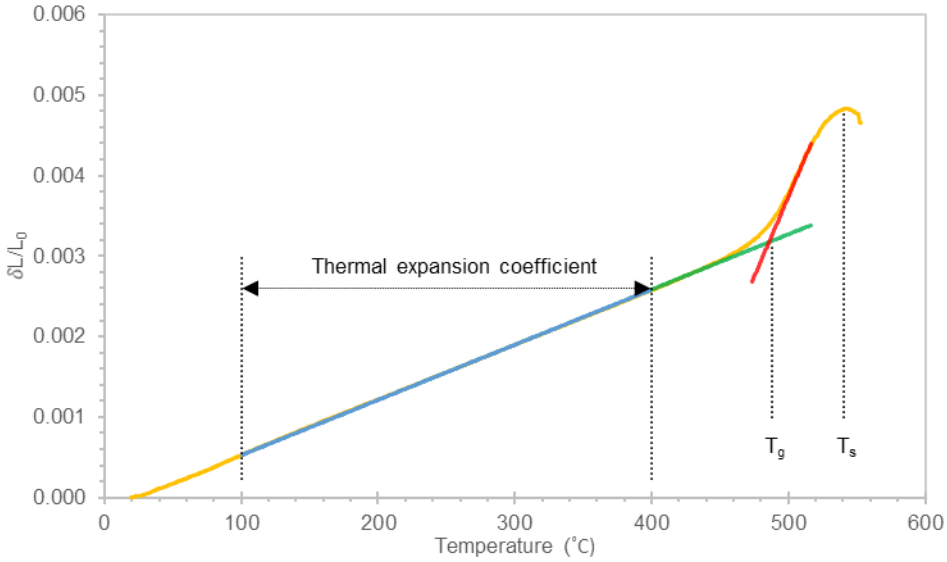

Figure 9.1 - Example of a dilatometric result.

UV-Vis absorption

A lambda 35 UV/Vis spectrophotometer by perkin-elmer was used, with 2 nm slits.

Steady-State Luminescence

Luminescence spectra were measured using a SPEX Fluorolog-3 Model FL3-22 spectrofluorimeter. 5 nm slits were used for the two dimensional spectra. Experiments were performed at room temperature 293 K, in a front face geometry

Time-Resolved Luminescence Spectra

The flash photolysis equipment used was an LKS.60 ns laser photolysis spectrometer from Applied Photophysics, with a Brilliant QSwitch Nd:YAG laser from Quantel, using the third harmonics (λex = 355 nm, laser pulse half-width equal to 6 ns).